# Distinct allosteric networks in CDK4 and CDK6 in the cell cycle and in drug resistance

Wengang Zhang,[1] Devin Bradburn,[2] Gretchen Heidebrink,[2] Yonglan Liu,[1] Hyunbum Jang,[1,3] and Ruth Nussinov [1,3,4*], Mardo Koivomagi[2, *]

[1]Cancer Innovation Laboratory, National Cancer Institute, Frederick, MD 21702, U.S.A.

[2]Laboratory of Biochemistry and Molecular Biology, National Cancer Institute, Bethesda, MD 20892, U.S.A.

[3]Computational Structural Biology Section, Frederick National Laboratory for Cancer Research, Frederick, MD 21702, U.S.A.

[4]Department of Human Molecular Genetics and Biochemistry, Sackler School of Medicine, Tel Aviv University, Tel Aviv 69978, Israel

* Author for correspondence: Mardo Koivomagi, Ruth Nussinov

**Email:** mardo.koivomagi@nih.gov NussinoR@mail.nih.gov

## Abstract

Cyclin-dependent kinases 4 and 6 (CDK4 and CDK6) are key regulators of the G1-S phase transition in the cell cycle. In cancer cells, CDK6 overexpression often outcompetes CDK4 in driving cell cycle progression, contributing to resistance against CDK4/6 inhibitors (CDK4/6i). This suggests distinct functional and conformational differences between these two kinases, despite their striking structural and sequence similarities. Understanding the mechanisms that differentiate CDK4 and CDK6 is crucial, as resistance to CDK4/6i—frequently linked to CDK6 overexpression—remains a significant therapeutic challenge. Notably, CDK6 is often upregulated in CDK4/6i-resistant cancers and rapidly proliferating hematopoietic stem cells, underscoring its unique regulatory roles. We hypothesize that their distinct conformational dynamics relate to the differences in the efficacy of their phosphorylation of retinoblastoma (Rb) protein inhibitor, and cell cycle control. This leads us to question *how their dissimilar conformational dynamics encode their distinct actions*. To elucidate their differential activities, molecular mechanisms, and inhibitor binding, we combine biochemical assays and molecular dynamics (MD) simulations. We discover that CDK4 and CDK6 have distinct allosteric networks connecting the β3-αC loop and the G-loop. CDK6 exhibits stronger coupling and shorter path lengths between these regions, resulting in higher kinase activity upon cyclin binding, suppressing Rb's activity, thus permitting cell cycle progression. We also discover an unrecognized role of CDK6 unstructured C-terminal part, which allosterically connects and stabilizes the R-spine, facilitating slightly higher activity. Our findings bridge structural similarity and functional divergence of CDK4 and CDK6, advancing the understanding of kinase regulation in cancer biology.



**Keywords:** $G_1$ cell cycle phase, $G_1$/S transition, cyclin-dependent kinases (CDKs), allosteric drug discovery, cancer, ligand binding, CDK inhibitor

## 1 | Introduction

The almost synonymous and interchangeable cyclin-dependent kinases 4 and 6 (CDK4 and CDK6), with relatively minor sequence and structural differences, differentially regulate the $G_1$-S phase transition of the cell cycle in CDK4/6 inhibitor (CDK4/6i)-resistant cancer cells, adult tissues, and hematopoietic stem cells (HSCs).[1-5] The crucial question of the molecular mechanisms by which overexpressed CDK6 in cancer resistant cells facilitate cell cycle progression— in lieu of CDK4— remains unanswered.

Cyclin dependent kinases (CDKs) and their regulatory subunits, cyclins, are essential in the ordered progression of cells through the cell cycle.[6] Dysregulation of cyclin-CDK complexes leads to uncontrolled cell growth, making them promising targets for anticancer therapies.[7] Closely evolutionarily related, CDK4 and CDK6 are activated by cyclin D binding and phosphorylation by CDK7 **(Fig. S1)**.**[8, 9]** The two share overlapping functions in regulating progression through $G_1$ by phosphorylating retinoblastoma protein (Rb).[10] Phosphorylation relieves Rb-mediated inhibition of E2F transcription factors, in turn stimulating expression of genes required for the transition into S-phase (such as cyclin E) and committing cells to replication **(Fig. 1A)**.[11] Because of their critical role in initiating the cell cycle, dual CDK4/6 inhibitors (palbociclib, abemaciclib, ribociclib) are used as chemotherapeutics in HR positive and HER2 negative breast cancer. However, their use is associated with a range of side effects, most notably neutropenia**.**[7, 12, 13] Hematopoietic stem cells (HSCs) rely on CDK6 to drive $G_1$ progression, whereas most cell types, including breast cancer cells, utilize CDK4. Despite their sequence and structural similarity, CDK4 and CDK6 differentially regulate $G_1$ progression in a variety of cell types and exhibit remarkable diversity in regulation, activation, and substrate recognition. In the case of rapidly dividing HSCs, the greater intrinsic catalytic activity of CDK6 may facilitate faster entry into the cell cycle. A CDK4 specific inhibitor, atirmociclib, has successfully been shown to halt breast cancer growth with reduced effect on neutrophil levels. However, an in depth understanding of the mechanistic differences between CDK4 and CDK6, which could inform better drug design,[14] has not yet been established. This is likely in part due to existing static structural analyses failing to capture allosteric networks which modulate the activity and substrate specificity through dynamic communication.[15] CDK4 and CDK6 likely rely on distinct allosteric pathways to mediate their unique functions, which may explain their specialized roles in the cell cycle and underlie differences in drug sensitivity.[16-20] These subtle structural differences may also underlie the development of drug resistance specifically through CDK6 overexpression. When in complex with the canonically inhibitory protein, INK4, CDK6 adopts a drug resistant yet ATP-binding competent state through which it can still sustain $G_1$ progression.[38] The differential response to inhibitors suggests distinct allosteric mechanisms of CDK4 and CDK6 which are not yet understood.[3, 7, 21-26]

Understanding these allosteric networks could be key to uncovering the unique mechanisms of these kinases and improved inhibitors.

Previously, our work resolved the question of how cyclin-D/CDK4 evolved to have *slower* catalytic phosphorylation in the long $G_1$ phase, whereas cyclin-E/CDK2 evolved to accomplish *fast* phosphorylation of its downstream targets during the short $G_1$-to-S transition timescale.[27, 28] We explained the mechanisms, on the conformational level, through which cyclin-D/CDK4 and cyclin-E/CDK2 complexes have adapted to their distinct functional requirements in the $G_1$ phase, and $G_1$/S phase transition, of the cell cycle. *We clarified why CDK2 can transition from its inactive to the active state faster than CDK4*,[29] *and how the $G_1$/S CDK2 complex can maintain faster phosphorylation rate than the $G_1$ CDK4 complex*.[30] We suggested the CDK2 structural features which are at play, including (i) stable G-loop, (ii) stable ATP binding site, (iii) stable hydrogen bonds between the hinge region and the adenosine ring of ATP, (iv) stronger protein-protein interactions between the kinase and its activating partner (cyclin) and (v), the stable hydrophobic R-spine that form the backbone of the kinase. These features are necessary but not sufficient for efficient catalysis. Building on these, here we explain how CDK4 and CDK6, despite sharing over 70% sequence identity, similar overall structures, and the same D-type cyclin partner, can exhibit certain distinct functional roles.

Here, we combine biochemical assays and molecular dynamics (MD) simulations analyses to dissect the distinct allosteric regulation of CDK4 and CDK6 and their drug resistance. We attribute the different activities of CDK4 and CDK6 to the local dynamics in the loops (β3-αC, β4-β5, G-loop) in the N-lobe. Our analysis shows that when engaged with cyclin-D, the β3-αC loop allosterically regulates the G-loop, a structure that caps the active site and is essential to kinase activity. In CDK6, the path length between the β3-αC loop and the G-loop is shorter, and the coupling strength between these regions is greater compared to CDK4, enhancing CDK6 activity. Of the few sequence differences between CDK4 and CDK6, the extra sequence in the C-terminus of CDK6 stands out, as it allosterically stabilizes the R-spine, enhancing its catalytic activity. This novel finding extends the long-standing understanding of the roles of the C-terminus in kinase activity,[31, 32] provides a deeper understanding of CDK4/6 function, and may guide the development of next-generation inhibitors.

## 2 | Materials and Methods

### Biochemical assays for kinase activity

#### Purification of cyclin/CDK complexes

Human cyclin-D1/CDK4/6 fusion complexes were purified from budding yeast cells using a FLAG affinity purification method, modified from a previous protocol.[33] Briefly, N-

terminally 3XFLAG-tagged cyclin/CDK fusions with a glycine-serine linker (3XGGGGS) were cloned into high-copy yeast vectors (pRS425) and overexpressed from the GAL1 promoter. The overexpressed 3XFLAG-tagged complexes were then purified by one-step immunoaffinity chromatography using ANTI-FLAG M2 affinity agarose beads (Sigma-Aldrich A2220) and eluted with 0.2 mg/mL 3XFLAG peptide (Sigma-Aldrich F4799).[34]

**Purification of substrate protein**

N-terminally 6His-tagged Rb C-terminal fragment (RbC) recombinant protein (aa: 772-928) was expressed in the *E. coli* strain BL21(DE3)RIL and the purification was performed using cobalt affinity chromatography. Proteins were eluted using buffer containing 25 mM HEPES pH 7.4, 300 mM NaCl, 10% glycerol, and 200 mM imidazole.

**In vitro kinase assay**

*In vitro* kinase assays were performed by incubating 1 µM RbC with cyclin-CDK fusion constructs (in the low nM range) in a reaction mixture containing 100 mM HEPES pH 7.4, 150 mM NaCl, 5 mM $MgCl_2$, ~0.02 mg/ml 3XFLAG peptide, 5% glycerol, 3 mM EGTA, 0.1 mg/ml BSA and 500 µM ATPγS. Reactions were quenched at 8 minutes by addition of EDTA to a final concentration of 25 mM. P-nitrobenzyl mesylate (pNBM) was added to a final concentration of 2 mM and incubated for >1 hour to alkylate thio-phosphorylated proteins. Reactions were separated on 12% SDS-PAGE gels and phosphorylation of substrate proteins was visualized by western blotting. Total protein levels were detected using Revert total protein stain (LiCOR; 926-11010). Western blots were performed using primary rabbit anti-thiophosphate ester antibody (1:2000; Abcam; ab92570) and mouse anti-FLAG antibody (1:5000; Sigma-Aldrich; F1804) coupled with donkey anti-rabbit 800CW and donkey anti-mouse 680CW antibody (1:12000; LiCOR). Fluorescent signal was detected using Odyssey CLX imager (LiCOR) and quantified with the ImageStudio Software (LiCOR). Data were analyzed using GraphPad Prism software (GraphPad). Kinase activity was determined by dividing phosphorylation signal (anti-thiophosphate ester) by both total RbC (detected via total protein staining) and total kinase (anti-FLAG) levels. The activity of all kinases was normalized relative to $CDK6^{WT}$, which was set to 1. Kinase activity, as determined from six independent experiments per enzyme, were compared using one-way ANOVA.

Inhibition assays were conducted as described above, except for the addition DMSO or inhibitor dissolved in DMSO at indicated concentrations. The final DMSO concentration was kept at 10%. Kinase activity was determined by dividing phosphorylation signal (anti-thiophosphate ester) by total RbC (detected via total protein staining) only. Data were fit by non-linear regression using the model “[Inhibitor] vs. response (three parameters)” to determine $IC_{50}$ values. $IC_{50}$ values from three independent experiments per drug-enzyme pair were compared using one-way ANOVA.

## Modeling of CDK complexes and their mutants

We modeled the conformations of the complexes of CDK4 and CDK6 in their cyclin-bound states in the presence of ATP. We constructed the initial coordinates of the active cyclin-D1/CDK4 complex using the crystal structures of cyclin-D3/CDK4 (PDB ID: 7SJ3), replacing the cyclin with cyclin-D1. Cyclin-D1 is modeled using PDB ID 2W9Z, with its C-terminus modeled using homology modeling based on that in cyclin-D3 from 7SJ3. The initial coordinates of cyclin-D1/CDK6 were modeled after the v-cyclin/CDK6 complex (PDB ID: 1XO2) with the cyclin replaced by the same cyclin-D1 as in the CDK4 complex. Both structures are phosphorylated at the active site of the A-loop (pT172 on CDK4, pT177 on CDK6). All missing loops were added using the CHARMM package. We also simulated the active conformations of both CDK4 and CDK6 monomers as well as the unphosphorylated A-loop, from their crystal structures listed above for reference. In all systems, ATP was loaded into both CDKs, replacing the inhibitors in the crystal structures of CDK4 in 7SJ3 and CDK6 in 1XO2 by aligning an ATP-bound crystal structure of CDK2 (PDB code: 1FIN) to both CDKs. The simulated CDK4 and CDK6 systems are listed in **Tables S1, S2**. The solvent was modeled using the TIP3P model with at least 15 Å shell of water in each direction of the periodic boundary box. The charge states of all titratable groups were set to reflect a neutral pH environment, with acidic side chains represented in their negatively charged forms and basic side chains in their positively charged forms. We added $Na^+$ and $Cl^-$ to neutralize the solvated systems and maintain a physiological salt concentration of 150 mM.

## MD simulation protocols

We performed MD simulations using methods similar to our previous works, in particular utilizing OpenMM.[35-41] The simulation process consisted of several steps up to the production run. We first performed energy minimization using OpenMM's minimization integrator for 10,000 steps to optimize the systems and remove unfavorable atomic contacts. For each system, we then executed three 2 μs all-atom explicit solvent MD simulations under the NPT ensemble (constant number of atoms, pressure, and temperature) with 3D periodic boundary conditions. We employed OpenMM version 8.1 for the production runs, utilizing the CHARMM 36m all-atom force field. [42-46] Temperature was maintained at 310 K using the Langevin integrator with a friction coefficient of 1 $ps^{-1}$. Pressure was kept constant at 1 atm using a Monte Carlo barostat with an update interval of 25 steps. We applied the SETTLE algorithm to constrain bonds involving hydrogen atoms, allowing for a 2-fs integration time step. Long-range electrostatic interactions were computed using the particle mesh Ewald (PME) method with a grid spacing of 0.1 nm. Short-range non-bonded interactions were calculated using a cutoff of 1.2 nm, with a switching function applied to van der Waals interactions starting at 1.0 nm. The simulations were run on CUDA-enabled GPUs to enhance computational efficiency. Trajectory frames were saved every 100 ps for subsequent analysis. We used

MDAnalysis, MDTraj and OpenMM's built-in analysis tools for post-processing and analyzing the simulation trajectories.[47, 48]

### Principal component analysis of protein dynamics

To analyze the large-scale motions of the protein during the MD simulation, we performed principal component analysis (PCA) using the Bio3D package in R(v4.4.0).[49, 50] PCA was conducted on the Cartesian coordinates of the Cα atoms to capture dominant motions and reduce the dimensionality of the trajectory. A covariance matrix was constructed from the atomic fluctuations of the Cα atoms around their mean positions. The covariance matrix captures the correlated motions of the atoms during the simulation. Next, eigenvalue decomposition of the covariance matrix was performed using the pca.xyz function to obtain eigenvalues and eigenvectors. The eigenvalues represent the variance explained by each principal component (PC), while the eigenvectors describe the direction of the motion in the conformational space. Then, the first few principal components (PCs) were analyzed in detail. Typically, the first few PCs capture the majority of the protein's collective motion. The contribution of each PC to the total motion was evaluated by the magnitude of the corresponding eigenvalue, and the cumulative variance was plotted to determine how many PCs are needed to describe the essential motions. To further determine the residues that contribute most to the dominant motions, the contribution of individual residues to each PC (loading plot) was calculated using Bio3D. The per-residue contribution was plotted to identify key regions of the protein involved in large-scale conformational changes.

### Community analysis

A network-based community analysis was conducted to identify clusters of residues that move collectively. The dynamic cross-correlation matrix (DCCM) was calculated using Bio3D to quantify correlated and anti-correlated motions between residue pairs. The Cα atom fluctuations from the MD trajectory were used to generate the DCCM. DCCM was then transformed into a distance matrix, and a protein structure network (PSN) was generated where nodes represent residues (Cα atoms), and edges represent significant correlations between them. The edges were weighted based on correlation strength, with a threshold set at 0.5 to filter noise. Communities were detected using the Girvan-Newman algorithm implemented in Bio3D, identifying groups of residues that share similar dynamic properties.

### Binding free energy calculations

To quantitatively evaluate the binding affinities and specificities between cyclin-D/CDK4 and cyclin-D/CDK6 complexes, we determined the binding free energies using the molecular mechanics/generalized Born surface area (MM/GBSA) approach, implemented

in AmberTools and Amber.[51] This method allows us to assess the interactions between cyclin-D and CDK4 or CDK6 by calculating the binding free energies from MD simulations of the complexes. The total binding free energy ($\Delta G_b$) is calculated as the sum of the molecular mechanics gas-phase energy ($\Delta E_{MM}$), solvation free energy ($\Delta G_{sol}$), and entropy contributions ($-T\Delta S$), where $T$ is the temperature (in Kelvin):

$$\langle \Delta G_{\mathrm{b}} \rangle = \langle \Delta E_{\mathrm{MM}} \rangle + \langle \Delta G_{\mathrm{sol}} \rangle - T\Delta S.$$

The ensemble averages, denoted by the angle brackets, were calculated over the final 1 μs of equilibrated configurations from the MD simulations. The components of the gas-phase molecular mechanics energy ($\Delta E_{MM}$) include the internal energy ($\Delta E_{inter}$), electrostatic interactions ($\Delta E_{elec}$), and van der Waals interactions ($\Delta E_{vdW}$):

$$\Delta E_{\mathrm{MM}} = \Delta H_{\mathrm{inter}} + \Delta H_{\mathrm{elec}} + \Delta H_{\mathrm{vdW}}.$$

The solvation free energy ($\Delta G_{sol}$) consists of the polar and nonpolar contributions, computed using the generalized Born (GB) model in AmberTools with the igb=5 parameter (GBneck2 model) for the polar solvation energy and a surface area-based model for the nonpolar component. The nonpolar contribution is calculated using the linear combination of pairwise overlap (LCPO) model:

$$\Delta G_{\mathrm{sol}} = \Delta G_{\mathrm{sol}}^{\mathrm{elec}} + \Delta G_{\mathrm{sol}}^{\mathrm{nonpolar}}.$$

The entropy contributions ($-T\Delta S$) to the binding free energy were estimated using normal mode analysis (NMODE) performed within AmberTools. These include translational ($T\Delta S_{trans}$), rotational ($T\Delta S_{rot}$), and vibrational ($T\Delta S_{vib}$) components. The vibrational contributions were computed from quasi-harmonic approximations based on the trajectory snapshots:

$$T\Delta S = T(\Delta S_{\mathrm{trans}} + \Delta S_{\mathrm{rot}} + \Delta S_{\mathrm{vib}}).$$

The net binding free energy ($\Delta G_b$) was determined by calculating the difference between the binding free energy of the bound complex and the sum of the free energies of the unbound CDK and cyclin proteins:

$$\Delta G_{\mathrm{b}} = \Delta G_{\mathrm{b}}^{\mathrm{complex}} - \left(\Delta G_{\mathrm{b}}^{\mathrm{CDK}} + \Delta G_{\mathrm{b}}^{\mathrm{cyclin}}\right)$$

**Allosteric pathway analysis**

To investigate allosteric pathways in our protein systems, we conducted a dynamical network analysis using the Bio3D package,[49] implementing the weighted implementation of suboptimal paths (WISP).[52] Each amino acid residue was treated as a node, with edges connecting residues whose Cα atoms were within a 5 Å threshold. Edge weights, $-\ln(c_{ij})$, where $c_{ij}$ is the correlation between residues forming the edge, are inversely proportional to the dynamic correlations calculated from MD simulations, indicating residue coupling strength. We selected source and sink residues based on

dynamic cross correlation and their functional relevance, typically involving key binding regions undergoing conformational changes during allosteric modulation. The path length is defined as the sum of edge weights along a path, with longer paths indicating weaker coupling between source and sink residues.

Using WISP, we calculated the top 100 suboptimal paths between source-sink pairs, capturing multiple communication routes and potential alternative pathways for signal propagation. Path lengths and their distributions were analyzed to assess coupling strength across the network. These analyses inform the protein's allosteric landscape, showing key residues mediating connectivity between functionally important sites.

### Quantification and statistical analysis

For statistical robustness, each complex was subjected to three independent MD simulations, with the final binding free energy values representing the average over these runs. The convergence of the simulations was assessed by monitoring the potential energy, electrostatic energy, and the root-mean-square deviation (RMSD) of the Cα atoms, ensuring that equilibrium was reached. To improve statistical accuracy, only the last 1 μs of each trajectory was used for energy calculations. Result analyses were carried out using OpenMM,[45, 46] VMD,[53] PyMOL,[54] MDAnalysis,[47] and custom Python scripts. All free energy results were reported as mean ± standard deviation across the independent simulation replicates.

## 3 | Results

### CDK6's longer C-terminus and CDK4's elongated β3-αC loop define its structural contrasts with CDK4

A high degree of functional and structural similarity has resulted in CDK4 and CDK6 often being referred to as "CDK4/6". However, both possess unique evolutionarily conserved structural features **(Fig. S2).** CDK6 has extended N- and C-termini, each containing an additional α-helix (αB and αJ) (**Fig. 1B-D)**. While the function of these extensions has yet to be investigated, in transcriptional CDKs, C-terminal extensions help to shape the active site.[55] CDK4 has a longer loop connecting its β3-strand to its αC-helix (β3-αC loop), $^{40}$PNGGGGGG$^{47}$ compared to $^{48}$QTGEE$^{52}$ in CDK6. Salt bridge formation between these two structural elements is required to form the ATP binding pocket, thus their relative positions are of critical importance in kinase activation.[29, 56] For example, decreasing the length of the β3-αC loop has been shown to lock BRAF in an active conformation and reduce inhibitor efficacy.[57] By contributing to distinct allosteric networks, these subtle structural variations may impart the distinct regulatory and functional properties of CDK4

and CDK6 in cell cycle control. This work explores the significance of these allosteric structural differences in relation to their activity and functional implications.

## Enhanced flexibility in CDK4 loops and C-lobe correlates with reduced activity

Despite only minor differences in sequence and structure between CDK4 and CDK6, biochemical assays reveal that wild-type CDK6 exhibits more than 10-fold greater kinase activity toward the Rb C-terminus (RbC) when compared to wild-type CDK4 (**Fig. 2A and S3**). To understand the structural origins of this difference, we performed principal component analysis (PCA) on the MD trajectories of cyclin-D/CDK4 and cyclin-D/CDK6. We denote these two systems $CDK4^{WT}$ and $CDK6^{WT}$. Analysis shows vastly different conformational clustering patterns for each kinase, with conformational ensembles depicted by PCA revealing distinct local fluctuation patterns for $CDK4^{WT}$ and $CDK6^{WT}$ in the first principal component in particular (**Fig. 2B**). The first two principal components explain a larger portion of the variance in $CDK4^{WT}$ (39%) than in $CDK6^{WT}$ (34%), suggesting greater conformational flexibility in $CDK4^{WT}$ (**Fig. 2C**). Residues in the β3-αC and β4-β5 loops display high degrees of conformational variability, as indicated by their contribution to PC1 (**Fig. 2D**). Conformational ensembles play a crucial role in determining function. [58, 59] Despite their sequence homology, CDK4 and CDK6 occupy different conformational spaces, likely reflecting their non-redundant functional roles in cell cycle progression.[17, 55, 60] This is consistent with findings that CDK6 has a more stable αC-helix conformation compared to CDK4, potentially explaining its higher basal activity.[61] The dynamic cross-correlation map for all residue pairs shows distinct patterns of intramolecular communication within $CDK4^{WT}$ and $CDK6^{WT}$ (**Fig. 2E**). $CDK4^{WT}$ shows more extensive anti-correlations between the N- and C-lobes. Excessive anti-correlation indicates less stable structure leading to lower efficiency compared to other cell cycle CDKs.[30]

## Longer β3-αC loop in CDK4 disrupts coordinated kinase dynamics and activity

$CDK4^{WT}$ has a longer and more flexible loop connecting the β3-strand to the αC-helix relative to $CDK6^{WT}$ (**Fig. 3A and 3B** and **Fig. S4**). During the transition from the inactive to the active state, the longer loops in CDK4 block the inward movement of the αC-helix upon cyclin binding, contributing to its slower activation compared to CDK2.[29] However, once CDK4 crosses the activation barrier and becomes the active complex (as in the state studied here), the β3-αC loop also plays a role in modulating the dynamics of the complex by decoupling the correlated motion of the αC-helix and the G-loop, hence decreasing the activity. The binding free energy indicates a stronger affinity between cyclin-D and $CDK6^{WT}$ compared to $CDK4^{WT}$ (**Fig. 3C**) due to more extensive contacts with cyclin-D (**Fig. S5**), resulting in the stronger coupling. This stronger association may contribute to the higher catalytic efficiency of CDK6, analogous to highly efficient cyclin-E and CDK2

having a greater binding affinity than cyclin-D and CDK4 in our previous study.[30] The flexible loop decreases binding affinity since flexibility increases the entropic contribution to the binding free energy, which decreases the binding affinity (**Fig. S6**).[62]

We next used community analysis to understand how the longer β3-αC loop in CDK4 affects the coordinated rearrangement of structural components essential for kinase activation. Community analysis, which segments proteins into smaller, interconnected groups of residues that move together as semi-rigid bodies, offers valuable insights into the cooperative dynamics of protein regions and the propagation of conformational changes throughout the structure. [15, 63-65] Structural analysis of the cyclin-D/CDK6$^{WT}$ complex places the G-loop and αC-helix in the same structural community, indicating coordinated movement between both structures (**Fig. 3E**). These structural elements play critical roles in facilitating catalysis, with the G-loop capping the active site and αC-helix ensuring that the kinase remains in an active state through its interactions with the β3-strand. Coordinated motion between the G-loop and αC-helix is associated with enhanced kinase activity, as seen in eukaryotic protein kinases.[66] Cyclin-D/CDK4$^{WT}$ lacks this coordination, as community analysis splits the G-loop and the αC-helix into different structural communities (**Fig. 3D**). This is at least partially due to the longer β3-αC loop in CDK4, as swapping the β3-αC loop in CDK6 for that of CDK4 (CDK6$^{\beta3\text{-}\alpha C(CDK4)}$) reduces catalytic activity by 50% and results in communities like those observed for CDK4$^{WT}$ (**Fig. 3F and S7**). Thus, this difference in dynamic organization may explain the higher basal activity observed in CDK6.

Finally, we assessed how the structural differences between CDK4 and CDK6 affects β3-strand αC-helix contacts. In active cyclin-CDK complexes, the β3-strand lysine (K35 in CDK4, K43 in CDK6) forms a salt bridge with the αC-helix aspartate (E56 in CDK4, E61 in CDK6) (**Fig. 3G**), creating a link to the G-loop, thereby stabilizing both elements. Our simulations reveal that CDK6$^{WT}$ has a far higher probability of salt bridge formation than CDK4$^{WT}$, suggesting a more efficient catalysis-ready conformation. Mutations affecting this residue disrupt the relative positioning of the G-loop and αC-helix, altering the active site and reducing catalytic efficiency.[66, 67] Given the importance of active site precision for efficient catalysis[67], coordinated motion between the G-loop and the αC-helix likely optimizes this conformation (**Fig. 3H**), leading to enhanced kinase activity.

**Stronger allosteric coupling in CDK6 stabilizes active site for efficient catalysis**

We next used network analysis to define the mechanism of allosteric regulation between the β3-αC loop and the G-loop. This network-based approach allows us to understand how signals travel through the kinase and how different structural elements work together *dynamically*. The strength of the connection between two residues is based on how

correlated their motions are: if they tend to move together, they form a path and are strongly connected. We focused on the allosteric signaling pathway linking the β3-αC loop (source) to the G-loop (sink) with source and sink residues selected based on the dynamic cross-correlation map (**Fig. 2E**). The selected source residues are G46 of CDK4 and E51 of CDK6 in the β3-αC loop and the sink residues are A16 of CDK4 and A23 of CDK6 in the G-loop.

The allosteric signaling path in $CDK4^{WT}$ is long and meandering, starting from its extended β3-αC loop and progressing through the β3-strand, β2-strand, and β1-strand before reaching to the G-loop (**Fig. 4A and C**). In contrast, the $CDK6^{WT}$ allosteric pathway is more direct, with the allosteric signal only passing through a small portion of the β3- and β2-strands without influencing the β1-strand (**Fig. 4B and E**). To investigate how strongly the residues along these paths are connected, we calculated the length of the allosteric path. The path length is the sum of edge weights in a network path connecting two sites, where each edge weight is typically calculated as $-\ln(|c_{ij}|)$ with $c_{ij}$ being the correlation between connected residues *i* and *j*, rather than the physical distance between the source and sink residues, or the number of residues between the source and sink along a path. The path length distribution in $CDK4^{WT}$ (peak at ~3.44) indicates slightly longer paths with weaker coupling between the source and sink residues compared to $CDK6^{WT}$ (peak at ~3.1) (**Fig. 4D and F**). The shorter allosteric path length in $CDK6^{WT}$ indicates stronger correlated motions between the β3-αC loop and the G-loop, potentially positively modulating the kinase activity. The different allosteric pathways can be attributed to the different length of the β3-αC loop. $CDK4^{WT}$ has a longer β3-αC loop than that of $CDK6^{WT}$ (**Fig. 1D)**. Loop swapping of $CDK6^{\beta3\text{-}\alpha C(CDK4)}$ by adopting the β3-αC loop of CDK4 results in longer allosteric paths, resembling those observed for $CDK4^{WT}$ (**Fig. S7**).

The G-loop connecting the β1- and β2-strands contains a conserved GxGxxG motif and is located on top of ATP, which is important for ATP positioning. Superimposition of the conformations from the simulated trajectories shows that the G-loop of $CDK4^{WT}$ has greater flexibility (**Fig. 4G**) compared to that of $CDK6^{WT}$ (**Fig. 4H**), as indicated by the residual RMSFs (**Fig. S9**). These observations could provide an explanation for the different responses of CDK4 and CDK6 to certain inhibitors, such as the CDK4-selective inhibitor atirmociclib (PF-07220060), which exhibits a remarkably high selectivity for CDK4 over CDK6. The enhanced flexibility of the CDK4 G-loop in part allows for more efficient binding of the bulky isopropyl alcohol [$(CH_3)_2COH$] group in this inhibitor (**Fig.**

**S10**).[68] Indeed, replacing the β3-αC loop in CDK6 with that of CDK4 ($CDK6^{\beta3\text{-}\alpha C(CDK4)}$) significantly increases its sensitivity to this CDK4-selective inhibitor (**Fig. 4I and S11)**.

### CDK6 C-terminus stabilizes the R-spine, enhancing catalytic activity

Relative to CDK4, CDK6 has an extended C-terminal tail, a structural feature known to regulate the kinase activity. For example, the C-terminal tail of PKA supports its active conformation.[31, 32] Some CDKs are known to have flexible C-terminal tail that helps to stabilize the N-lobe by folding onto it, enclosing the ATP in its active site.[55] However, it is not known how the C-terminal tail of CDK6 affects its conformational dynamics. To elucidate the role of the C-terminus, we simulated CDK6 with a truncated C-terminal tail ($CDK6^{\Delta Cterm}$) and calculated the cross-correlation of atomic fluctuations. The dynamic cross-correlation map reveals highly correlated residue motions between the N- and C-lobes of $CDK6^{WT}$ (**Fig. 5A and C**). In contrast, these residue motions are uncorrelated in $CDK6^{\Delta Cterm}$ (**Fig. 5B**). Instead, correlation is primarily observed within the C-lobe (**Fig. 5D**). We hypothesize that in $CDK6^{\Delta Cterm}$, the absence of the correlated residue pairs between the N- and C-lobes renders the inter-lobe motions rigid, hindering the opening and closing of the active site and resulting in lower activity. Consistent with this, biochemical assays with $CDK6^{\Delta Cterm}$ show reduced kinase activity compared to $CDK6^{WT}$, resulting in a lower rate of RbC phosphorylation (**Fig. 5E**). One explanation for the reduced activity of $CDK6^{\Delta Cterm}$ is that the C-terminal deletion disrupts the coordinated movements of the regulatory-spine (R-spine) of CDK6 (**Fig. 5F**). Once the R-spine is disrupted, the kinase is less likely to maintain its stability and resulting in reduced activity.[69] In $CDK6^{WT}$, we observed multiple strong and short allosteric signaling paths connecting the C-terminal edge of the kinase domain to an R-spine residue (**Fig. 5G**), but this is not the case in $CDK6^{\Delta Cterm}$ (**Fig. 5H**). $CDK6^{\Delta Cterm}$ disrupts the intrinsic dynamics of the kinase, resulting in longer allosteric paths from the C-terminus through both αH- and αF-helices to the R-spine. This is in part due to the high mobility of the truncated C-terminal tail (**Fig. S12**), which increases the dynamics of the C-lobe, breaking the intrinsic coordinated motions within the kinase that separate R-spine into three distinct communities (**Fig. 5F**). Our finding represents a novel mechanism of kinase activity in which the C-terminal tail plays a direct role in modulating the opening and closing of the C- and N-lobes through R-spine dynamics.

## 4 | Discussion

Though largely identical, CDK4 and CDK6 evolved distinct activities in regulating the $G_1$ progression. This distinction is particularly relevant to CDK4/6 inhibitor-resistant cancer

cells, adult tissues, and HSCs. The key question is how the overexpressed CDK6 in cancer cells enables cell cycle progression in lieu of CDK4, and what molecular mechanisms differentiate the higher activity of CDK6 from that of CDK4. Explaining these differences at the conformational level could clarify the shifts towards the CDK6 complex for cell cycle progression in resistant cancer cells, thereby bypassing CDK4/6 inhibition.

Our experimental results indicate that $CDK6^{WT}$ is more active than $CDK4^{WT}$ and $CDK6^{\Delta Cterm}$. The latter, which lacks the C-terminal part of CDK6 is more similar to CDK4 in terms of activity. We use MD simulations to explain the molecular origin of their catalytic differences. The higher activity of $CDK6^{WT}$ can be attributed to several factors, including firstly, the allosteric role of the β3-αC loop upon cyclin binding. A longer β3-αC loop in CDK4 results in a *disjointed* kinase, while a shorter loop in CDK6 is better at facilitating *coordinated* motion for efficient catalysis. Furthermore, the weaker coupling between the G-loop and the β3-αC loop in $CDK4^{WT}$ allows decoupling of the β-stands (β1-β5) and the αC-helix. This results in insufficient stabilization of ATP and, consequently, lower activity due to the longer β3-αC loop of $CDK4^{WT}$. In contrast, $CDK6^{WT}$ has a shorter β3-αC loop, resulting in stronger coupling between the G-loop and the β3-αC loop. This enhanced coupling leads to better stabilization of ATP and higher catalytic activity. Secondly, the unstructured C-terminus of $CDK6^{WT}$ acts on the kinase allosterically, stabilizing the R-spine for more efficient catalysis. In contrast, $CDK4^{WT}$ lacks this C-terminus, leading to a less stable R-spine, as shown in our previous works.[30] Thirdly, the dynamics of $CDK4^{WT}$ reveal a significant degree of opening and closing of the N- and C-lobes, leading to an unstable structure as evidenced by the unstable R-spine.[30] This instability likely contributes to the slower catalytic activity observed for CDK4, as the excessive conformational changes typically hinder efficient substrate binding and phosphoryl transfer (**Fig. 6**). In contrast, as discussed in our previous work,[30] $CDK2^{WT}$ displayed a relatively stable structure with less dynamic opening and closing motions of the N- and C-lobes for ATP binding, resulting in higher catalytic activity. We suspect that $CDK6^{WT}$ may exhibit the right balance of N- and C-lobe movements between CDK2 and CDK4, and a coordinated and efficient catalytic process. The ability of $CDK6^{WT}$ to maintain a dynamic yet stable conformation is likely responsible for its higher activity compared to both $CDK4^{WT}$ and $CDK6^{\Delta Cterm}$.

These findings suggest that achieving optimal kinase function requires the right balance of conformational plasticity and show that the evolution of CDK6, as exemplified by its role in fast-proliferating short-term HSCs, has favored allosteric networks that enhance its activity relative to CDK4. In CDK4/6i-resistant cancer cells, CDK6 is often overexpressed. When complexed with CIP/KIP family inhibitors, such as p18 or p27, CDK6 becomes insensitive to the inhibitors, in part due to the allosteric mechanisms it has acquired through evolution.[23, 61] These mechanisms include the longer C-

terminus, which stabilizes the R-spine, and stronger coupling between the β3-αC loop and the αC-helix upon cyclin binding.

The divergence in sequence, function, and activity of CDK4 and CDK6 is not unique in evolution, and our results show that such differences provide opportunities for designing inhibitors that selectively target one kinase but not the other. Notably, FGFR1 and FGFR2 follow a similar pattern.[70, 71] Despite their high sequence similarity, these kinase pairs exhibit different catalytic efficiencies and regulatory mechanisms. The different dynamics of FGFR1 and FGFR2 have been leveraged in the design of the inhibitor lirafugratinib to selectively target FGFR2.[71] The G-loop (or P-loop) in FGFR1 is highly flexible, rapidly transitioning between an extended conformation and a more contracted state. In contrast, the G-loop in FGFR2 maintains a relatively extended conformation, which is far less dynamic than that of FGFR1, allowing efficient covalent binding of lirafugratinib to C491 in FGFR2. Although lirafugratinib stabilizes the G-loop conformation in FGFR1, the covalent bond is too far away from C488 for efficient covalent binding. These examples show the importance of considering protein dynamics in drug design.

Closely related kinases, such as CDK4 and CDK6, often have different allosteric mechanisms that can potentially be exploited to selectively target one over the other. For example, AKT1 is more biochemically active and responsible for the tumor initiation, while AKT2 is mainly responsible for tumor progression and metastasis.[72] Their divergence is in part allosterically regulated by their differences in the PH domain.[73]

Here, we discover two novel allosteric mechanisms that CDK4 and CDK6 utilize to differentially regulate their activity: allosteric signaling between the β3-αC loop and the G-loop, “sensing” cyclin binding, and the C-terminus of CDK6, modulating its activity through coordinated R-spine movement. The weak allosteric coupling of β3-αC loop and G-loop in the CDK4 offers a more flexible G-loop compared to CDK6. These allosteric mechanisms may also in part explain why overexpression of CDK6, rather than CDK4, leads to drug resistance. This is because CDK6 may be more efficient at promoting cell cycle progression even when partially inhibited, and the relatively inflexible G-loop of CDK6 is less likely to allow binding of bigger ligands such as inhibitors, while simultaneously allowing binding and unbinding of ATP, facilitating ATP hydrolysis.[23, 74] To overcome CDK6 overexpression in drug resistance to CDK4/6i, proteolysis-targeting chimeras (PROTACs) and molecular glue degraders have been proposed.[60, 74] This

strategy is highly promising as it potentially eliminates the overexpressed CDK6 through its targeted degradation, rather than merely inhibiting its activity.

## 5 | Conclusions

Our combined approach, leveraging molecular simulations and biochemical assays, uncovers new molecular mechanisms underlying the allosteric differences between the closely related CDK4 and CDK6.Two allosteric networks are identified: one in the N-lobe (connecting the β3-αC loop and G-loop) and another in the C-lobe (linking the C-terminus and R-spine). In CDK6 these networks have shorter paths or stronger coupling than those in CDK4, providing favorable conditions for higher kinase activity. These findings reveal how these kinases evolved to fulfill distinct functional roles in different cell types and offer new mechanistic details into their allosteric regulation and inhibitor specificity.

## Acknowledgments

This project was supported in whole or in part by federal funds from the National Cancer Institute, National Institutes of Health, under contract HHSN261201500003I. The contents of this publication do not necessarily reflect the views or policies of the Department of Health and Human Services, nor does mention of trade names, commercial products, or organizations imply endorsement by the U.S. government. This research was supported [in part] by the Intramural Research Program of the NIH, National Cancer Institute, Center for Cancer Research. All simulations had been performed using the high-performance computational facilities of the Biowulf cluster at the National Institutes of Health, Bethesda, MD (https://hpc.nih.gov/).

## Conflict of interest

The author declares that there is no conflict of interest that could be perceived as prejudicing the impartiality of the research reported.

## Figure captions

**Figure 1. CDK4 and CDK6 domain structures and sequence alignments.**
(A) Cell cycle and $G_1$-S phase signaling pathway. CDK4 and CDK6 are essential in regulating the $G_1$ phase of the cell cycle. When complexed with cyclin-D (Cyc D), they phosphorylate Rb, partially releasing E2F transcription factors to induce cyclin-E expression. Cyclin-E/CDK2 then completes Rb phosphorylation, fully releasing E2F, and

driving cells into the S phase. The pathway shows the cooperative roles of CDK4/6 and CDK2 in promoting cell cycle progression through a positive feedback loop.
(B) Domain structure of CDK4 and CDK6; both CDK4 and CDK6 share a kinase domain but differ in their N-terminal αB-helix and C-terminal αJ-helix regions.
(C) Structural alignment of CDK4 and CDK6. The 3D structures of CDK4 (cyan, PDB ID: 7SJ3) and CDK6 (pink, PDB ID: 1XO2) are superimposed, revealing overall similarity with some differences in specific regions. The red circle highlights the β3-αC loop, where structural divergence is observed.
(D) Sequence alignment of CDK4 and CDK6 highlights conserved residues (purple background) and divergent residues (white background). Key secondary structures, including α-helices (αB, αC, αD, etc.) and β-strands (β1, β2, etc.), are annotated. Differences in the N-terminal αB helix and C-terminal αJ helix are marked with red boxes, while variations in the β3-αC loop are emphasized with dashed boxes, corresponding to structural discrepancies shown in panel C. CDK6 contains seven additional residues in the N-terminus and 23 extra residues in the C-terminus, including the αJ helix, which is absent in CDK4.

**Figure 2. CDK6$^{WT}$ is more active than CDK4$^{WT}$, in part due to its lower local dynamics in β3-αC and β4-β5, and G-loops.**
(A) Normalized kinase activity of cyclin D1-CDK6$^{WT}$ and cyclin D1-CDK4$^{WT}$ fusions toward RbC. (N = 5-6; ****P<0.0001)
(B) Tube representations of the first principal component (PC1) from PCA of CDK4$^{WT}$ and CDK6$^{WT}$. Color gradients represent mode mobility, from immobile (blue) to highly mobile (red). Notable dynamic regions include the β3-αC, β4-β5, and β2-β3, and G-loops. ATP is shown bound in the active site. The binding cyclins are not displayed for visual clarity.
(C) PCA plot for the first and second principal component (PC1 and PC2) of CDK4$^{WT}$ and CDK6$^{WT}$, show distinct clustering patterns. For CDK4$^{WT}$, PC1 and PC2 account for 27.78% and 11.23% of the total variance, respectively. For CDK6$^{WT}$, PC1 and PC2 explain 23.88% and 10.45% of the total variance, respectively. Each dot represents one

snapshot from the trajectories in the plot. The color ranging from blue to red represents the trajectory frame from beginning to end.
(D) PC1 loading plots for $CDK4^{WT}$ and $CDK6^{WT}$. The fluctuation profiles identify regions of high conformational variability, particularly in the β3-αC and β4-β5 loops. β3-αC loop has more significant contribution to the PC1 than that of CDK6.
(E) Dynamic cross-correlation maps for $CDK4^{WT}$ and $CDK6^{WT}$. Positive correlations (magenta) and anti-correlations (cyan) highlight coupled motions between specific regions.

**Figure 3. Longer β3-αC loop of CDK4 is the key in the binding interface between CDK4 and cyclin-D and decouples N-lobe β-strands and αC-helix, negatively regulating their activities.**
(A) Sequence alignment of the β3-αC loop region in CDK4 and CDK6. This panel shows the β3-αC loop of CDK4 has a significantly longer sequence of glycine residues than CDK6.
(B) Structural overlay of flexible β3-αC loop region from the trajectories of $CDK4^{WT}$. The overlay demonstrates the highly mobile nature of the β3-αC loop in $CDK4^{WT}$.
(C) Binding free energy ($\Delta G^{CycD}$) of cyclin-D with $CDK4^{WT}$ and $CDK6^{WT}$. The bars represent the calculated ΔG for the binding of cyclin-D to wild-type CDK4 (left, blue) and wild-type CDK6 (right, purple). More negative values indicate stronger binding, with error bars representing the standard deviations.
Community network of (D) cyclin-D/$CDK4^{WT}$ and (E) cyclin-D/$CDK6^{WT}$ complexes. In the CDK4 complex (D), the G-loop and αC-helix are in different communities, whereas in the CDK6 complex (E), they are in the same community. Different colors of the cartoon representation of CDKs represent distinct communities.
(F) Normalized kinase activity of cyclin D1-$CDK6^{WT}$ and cyclin D1-$CDK6^{\beta3\text{-}\alpha C(CDK4)}$ fusions toward RbC. (N = 6; ****P<0.0001)
(G) Probability of β3-Lys and αC-Glu salt bridge formation. This bar graph shows the higher probability of the formation of the β3-Lys and αC-Glu salt bridge in $CDK6^{WT}$ compared to $CDK4^{WT}$. The higher probability in $CDK6^{WT}$ suggests more stable active conformation.
(H) Snapshot highlighting the Lys-Glu salt bridge in $CDK6^{WT}$. This conformation is characteristic of the active conformation of kinases.

**Figure 4. Allosteric signaling pathways between the β3-αC loop and the G-loop.**
Optimal (red lines) and sub-optimal (blue lines) allosteric paths for (A) $CDK4^{WT}$, and (B) $CDK6^{WT}$. The allosteric signaling pathway starting from the β3-αC loop to G-loop of CDK4

follows a longer path than that of CDK6. The green spheres are α-carbon of residues and represent nodes in the allosteric pathways.
(C) Schematic illustration of the optimal allosteric paths and (D) path length distribution between the source and sink residues for $CDK4^{WT}$.
(E) Schematic illustration of the optimal allosteric paths and (F) path length distribution between the source and sink residues for $CDK6^{WT}$. Shorter path length suggests a stronger allosteric pathway between the source and sink.
Overlay of simulation trajectories for (G) $CDK4^{WT}$ and (H) $CDK6^{WT}$. G-loop (green) of CDK4 is longer than that of CDK6 and is more dynamic.
(I) $IC_{50}$ values for palbociclib and atirmociclib mediated inhibition of cyclin D1-$CDK6^{WT}$ (11.17 ± 1.51 nM and 79.69 ± 13.23 nM) and cyclin D1-$CDK6^{\beta3\text{-}\alpha C(CDK4)}$ (15.22 ± 4.66 nM and 12.18 ± 5.84 nM). (N = 3; **P<0.005)

**Figure 5. C-terminus modulates the C- and N-lobe opening and closing of CDK6 facilitating more efficient catalysis.**
Dynamic cross-correlation maps of residue for (A) $CDK6^{WT}$ and (B) $CDK6^{\Delta Cterm}$. The maps use a color scale from cyan (-1.0, anti-correlated) to magenta (+1.0, correlated) to show how different protein residues move in relation to each other. A key difference is highlighted in the circled region, showing distinct correlation patterns between N-lobe (residues 1-100) and C-lobe (residues >100) movements in the two kinases.
Tube representations of the most correlated and anti-correlated motion in (C) $CDK6^{WT}$ and (D) $CDK6^{\Delta Cterm}$. These panels show the regions of $CDK6^{WT}$ and $CDK6^{\Delta Cterm}$ with the most correlated (positive correlations, red) and anti-correlated (negative correlations, blue) motions, showing how the truncation of the C-terminus alters these dynamics.
(E) Normalized kinase activity of cyclin D1-$CDK6^{WT}$ and cyclin D1-$CDK6^{\Delta Cterm}$ fusions toward RbC. (N = 6; ****P<0.0001)
(F) Structural community analysis of $CDK6^{WT}$ and $CDK6^{\Delta Cterm}$ focusing on the regulatory spine (R-spine). In $CDK6^{WT}$, the R-spine residues (L79, L65, F164, H143) form a single cohesive community (orange), while in $CDK6^{\Delta Cterm}$, these residues are dispersed across three different communities (colored differently), suggesting compromised structural integrity.
Allosteric pathway analysis in (G) $CDK6^{WT}$ and (H) $CDK6^{\Delta Cterm}$. The graphs trace the communication pathway (highlighted in various colors) from the source residue E308 in the C-terminal region to the sink residue H143 in the R-spine. $CDK6^{WT}$ shows a direct

pathway through the αE-helix, while $CDK6^{\Delta Cterm}$ exhibits a longer route through multiple helices (αH and αF), indicating altered internal dynamics due to C-terminal truncation.

**Figure 6. CDK4 and CDK6 dynamic divergence gives rise to their distinct activity.** (A) Schematic of cell cycle showing CDK-cyclin complex activity at different phases ($G_1$, S, G2, M). Gradient scales show that $CDK4^{WT}$ exhibits higher flexibility but lower phosphorylation rate, while $CDK6^{WT}$ shows lower flexibility but higher phosphorylation rate. This inverse relationship between flexibility and catalytic efficiency reflects the evolutionary adaptation of CDK6 for rapid cell division in stem-like cells like ST-HSC cells. (B) Structural comparison of $CDK4^{WT}$ and $CDK6^{WT}$ highlighting key differences in their regulatory mechanisms. $CDK4^{WT}$ has a longer β3-αC loop that results in weak allosteric coupling between αC-helix and the G-loop, while CDK6 has a shorter β3-αC loop with a stronger allosteric coupling, and its C-terminus stabilizes the R-spine for more efficient phosphorylation.

## References


1. Bockstaele, L., Bisteau, X., Paternot, S. & Roger, P. P. (2009). Differential regulation of cyclin-dependent kinase 4 (CDK4) and CDK6, evidence that CDK4 might not be activated by CDK7, and design of a CDK6 activating mutation. Mol Cell Biol. **29**, 4188-4200. https://doi.org/10.1128/MCB.01823-08.
2. Fassl, A., Geng, Y. & Sicinski, P. (2022). CDK4 and CDK6 kinases: From basic science to cancer therapy. Science. **375**, eabc1495. https://doi.org/10.1126/science.abc1495.
3. Glaviano, A., Wander, S. A., Baird, R. D., Yap, K. C., Lam, H. Y., Toi, M., Carbone, D., Geoerger, B., Serra, V., Jones, R. H., Ngeow, J., Toska, E., Stebbing, J., Crasta, K., Finn, R. S., Diana, P., Vuina, K., de Bruin, R. A. M., Surana, U., Bardia, A. & Kumar, A. P. (2024). Mechanisms of sensitivity and resistance to CDK4/CDK6 inhibitors in hormone receptor-positive breast cancer treatment. Drug Resist Updat. **76**, 101103. https://doi.org/10.1016/j.drup.2024.101103.
4. Hu, A. J., Li, W., Pathak, A., Hu, G. F., Hou, X., Farmer, S. R. & Hu, M. G. (2023). CDK6 is essential for mesenchymal stem cell proliferation and adipocyte differentiation. Front Mol Biosci. **10**, 1146047. https://doi.org/10.3389/fmolb.2023.1146047.
5. Ng, Y. L. D., Ramberger, E., Bohl, S. R., Dolnik, A., Steinebach, C., Conrad, T., Müller, S., Popp, O., Kull, M., Haji, M., Gütschow, M., Döhner, H., Walther, W., Keller, U., Bullinger, L., Mertins, P. & Krönke, J. (2022). Proteomic profiling reveals CDK6 upregulation as a targetable resistance mechanism for lenalidomide in multiple myeloma. Nature Communications. **13**. https://doi.org/10.1038/s41467-022-28515-1.
6. Morgan, D. O. (2007). The cell cycle: principles of control. New Science Press.
7. Morrison, L., Loibl, S. & Turner, N. C. (2024). The CDK4/6 inhibitor revolution - a game-changing era for breast cancer treatment. Nat Rev Clin Oncol. **21**, 89-105. https://doi.org/10.1038/s41571-023-00840-4.
8. Harbour, J. W., Luo, R. X., Dei Santi, A., Postigo, A. A. & Dean, D. C. (1999). Cdk phosphorylation triggers sequential intramolecular interactions that progressively block Rb functions as cells move through G1. Cell. **98**, 859-869. https://doi.org/10.1016/s0092-8674(00)81519-6.
9. Schachter, M. M., Merrick, K. A., Larochelle, S., Hirschi, A., Zhang, C., Shokat, K. M., Rubin, S. M. & Fisher, R. P. (2013). A Cdk7-Cdk4 T-Loop Phosphorylation Cascade Promotes G1 Progression. Molecular Cell. **50**, 250-260. https://doi.org/10.1016/j.molcel.2013.04.003.
10. Topacio, B. R., Zatulovskiy, E., Cristea, S., Xie, S., Tambo, C. S., Rubin, S. M., Sage, J., Koivomagi, M. & Skotheim, J. M. (2019). Cyclin D-Cdk4,6 Drives Cell-Cycle Progression via the Retinoblastoma Protein's C-Terminal Helix. Mol Cell. **74**, 758-770 e754. https://doi.org/10.1016/j.molcel.2019.03.020.
11. Chellappan, S. P., Hiebert, S., Mudryj, M., Horowitz, J. M. & Nevins, J. R. (1991). The E2F transcription factor is a cellular target for the RB protein. Cell. **65**, 1053-1061. https://doi.org/10.1016/0092-8674(91)90557-f.
12. Beaver, J. A., Amiri-Kordestani, L., Charlab, R., Chen, W., Palmby, T., Tilley, A., Zirkelbach, J. F., Yu, J., Liu, Q., Zhao, L., Crich, J., Chen, X. H., Hughes, M., Bloomquist, E., Tang, S., Sridhara, R., Kluetz, P. G., Kim, G., Ibrahim, A., Pazdur, R. & Cortazar, P. (2015). FDA Approval: Palbociclib for the Treatment of Postmenopausal Patients with Estrogen Receptor-Positive, HER2-Negative Metastatic Breast Cancer. Clin Cancer Res. **21**, 4760-4766. https://doi.org/10.1158/1078-0432.CCR-15-1185.
13. Shah, A., Bloomquist, E., Tang, S., Fu, W., Bi, Y., Liu, Q., Yu, J., Zhao, P., Palmby, T. R., Goldberg, K. B., Chang, C. J. G., Patel, P., Alebachew, E., Tilley, A., Pierce, W. F., Ibrahim, A., Blumenthal, G. M., Sridhara, R., Beaver, J. A. & Pazdur, R. (2018). FDA Approval: Ribociclib for the Treatment of Postmenopausal Women with Hormone Receptor-Positive, HER2-Negative Advanced or Metastatic Breast Cancer. Clin Cancer Res. **24**, 2999-3004. https://doi.org/10.1158/1078-0432.CCR-17-2369.
14. Liu, Y., Zhang, M., Jang, H. & Nussinov, R. (2024). The allosteric mechanism of mTOR activation can inform bitopic inhibitor optimization. Chem Sci. **15**, 1003-1017. https://doi.org/10.1039/d3sc04690g.
15. Masterson, L. R., Mascioni, A., Traaseth, N. J., Taylor, S. S. & Veglia, G. (2008). Allosteric cooperativity in protein kinase A. Proc Natl Acad Sci U S A. **105**, 506-511. https://doi.org/10.1073/pnas.0709214104.
16. Uhlen, M., Fagerberg, L., Hallstrom, B. M., Lindskog, C., Oksvold, P., Mardinoglu, A., Sivertsson, A., Kampf, C., Sjostedt, E., Asplund, A., Olsson, I., Edlund, K., Lundberg, E., Navani, S., Szigyarto, C. A., Odeberg, J., Djureinovic, D., Takanen, J. O., Hober, S., Alm, T., Edqvist, P. H., Berling, H., Tegel, H., Mulder, J.,

Rockberg, J., Nilsson, P., Schwenk, J. M., Hamsten, M., von Feilitzen, K., Forsberg, M., Persson, L., Johansson, F., Zwahlen, M., von Heijne, G., Nielsen, J. & Ponten, F. (2015). Proteomics. Tissue-based map of the human proteome. Science. **347**, 1260419. https://doi.org/10.1126/science.1260419.

17. Ameratunga, M., Kipps, E., Okines, A. F. C. & Lopez, J. S. (2019). To Cycle or Fight—CDK4/6 Inhibitors at the Crossroads of Anticancer Immunity. Clin Cancer Res. **25**, 21-28. https://doi.org/10.1158/1078-0432.Ccr-18-1999.
18. Laurenti, E., Frelin, C., Xie, S., Ferrari, R., Dunant, C. F., Zandi, S., Neumann, A., Plumb, I., Doulatov, S., Chen, J., April, C., Fan, J. B., Iscove, N. & Dick, J. E. (2015). CDK6 levels regulate quiescence exit in human hematopoietic stem cells. Cell Stem Cell. **16**, 302-313. https://doi.org/10.1016/j.stem.2015.01.017.
19. Scheicher, R., Hoelbl-Kovacic, A., Bellutti, F., Tigan, A. S., Prchal-Murphy, M., Heller, G., Schneckenleithner, C., Salazar-Roa, M., Zochbauer-Muller, S., Zuber, J., Malumbres, M., Kollmann, K. & Sexl, V. (2015). CDK6 as a key regulator of hematopoietic and leukemic stem cell activation. Blood. **125**, 90-101. https://doi.org/10.1182/blood-2014-06-584417.
20. Rodriguez-Diez, E., Quereda, V., Bellutti, F., Prchal-Murphy, M., Partida, D., Eguren, M., Kollmann, K., Gomez de Cedron, M., Dubus, P., Canamero, M., Martinez, D., Sexl, V. & Malumbres, M. (2014). Cdk4 and Cdk6 cooperate in counteracting the INK4 family of inhibitors during murine leukemogenesis. Blood. **124**, 2380-2390. https://doi.org/10.1182/blood-2014-02-555292.
21. Huang, J., Zheng, L., Sun, Z. & Li, J. (2022). CDK4/6 inhibitor resistance mechanisms and treatment strategies (Review). Int J Mol Med. **50**. https://doi.org/10.3892/ijmm.2022.5184.
22. Stanciu, I.-M., Parosanu, A. I., Orlov-Slavu, C., Iaciu, I. C., Popa, A. M., Olaru, C. M., Pirlog, C. F., Vrabie, R. C. & Nitipir, C. (2023). Mechanisms of Resistance to CDK4/6 Inhibitors and Predictive Biomarkers of Response in HR+/HER2-Metastatic Breast Cancer—A Review of the Literature. Diagnostics. **13**. https://doi.org/10.3390/diagnostics13050987.
23. Li, Q., Jiang, B., Guo, J., Shao, H., Del Priore, I. S., Chang, Q., Kudo, R., Li, Z., Razavi, P., Liu, B., Boghossian, A. S., Rees, M. G., Ronan, M. M., Roth, J. A., Donovan, K. A., Palafox, M., Reis-Filho, J. S., de Stanchina, E., Fischer, E. S., Rosen, N., Serra, V., Koff, A., Chodera, J. D., Gray, N. S. & Chandarlapaty, S. (2022). INK4 Tumor Suppressor Proteins Mediate Resistance to CDK4/6 Kinase Inhibitors. Cancer Discov. **12**, 356-371. https://doi.org/10.1158/2159-8290.CD-20-1726.
24. Yang, C., Li, Z., Bhatt, T., Dickler, M., Giri, D., Scaltriti, M., Baselga, J., Rosen, N. & Chandarlapaty, S. (2017). Acquired CDK6 amplification promotes breast cancer resistance to CDK4/6 inhibitors and loss of ER signaling and dependence. Oncogene. **36**, 2255-2264. https://doi.org/10.1038/onc.2016.379.
25. Cornell, L., Wander, S. A., Visal, T., Wagle, N. & Shapiro, G. I. (2019). MicroRNA-Mediated Suppression of the TGF-beta Pathway Confers Transmissible and Reversible CDK4/6 Inhibitor Resistance. Cell Rep. **26**, 2667-2680 e2667. https://doi.org/10.1016/j.celrep.2019.02.023.
26. Venkataramani, R., Swaminathan, K. & Marmorstein, R. (1998). Crystal structure of the CDK4/6 inhibitory protein p18INK4c provides insights into ankyrin-like repeat structure/function and tumor-derived p16INK4 mutations. Nat Struct Biol. **5**, 74-81. https://doi.org/10.1038/nsb0198-74.
27. Nussinov, R., Zhang, W., Liu, Y. & Jang, H. (2024). Mitogen signaling strength and duration can control cell cycle decisions. Sci Adv. **10**, eadm9211. https://doi.org/10.1126/sciadv.adm9211.
28. Fagundes, R. & Teixeira, L. K. (2021). Cyclin E/CDK2: DNA Replication, Replication Stress and Genomic Instability. Front Cell Dev Biol. **9**, 774845. https://doi.org/10.3389/fcell.2021.774845.
29. Zhang, W., Liu, Y., Jang, H. & Nussinov, R. (2024). Slower CDK4 and faster CDK2 activation in the cell cycle. Structure. **32**, 1269-1280 e1262. https://doi.org/10.1016/j.str.2024.04.012.
30. Zhang, W., Liu, Y., Jang, H. & Nussinov, R. (2024). CDK2 and CDK4: Cell Cycle Functions Evolve Distinct, Catalysis-Competent Conformations, Offering Drug Targets. JACS Au. **4**, 1911-1927. https://doi.org/10.1021/jacsau.4c00138.
31. Taylor, S. S., Soberg, K., Kobori, E., Wu, J., Pautz, S., Herberg, F. W. & Skalhegg, B. S. (2022). The Tails of Protein Kinase A. Mol Pharmacol. **101**, 219-225. https://doi.org/10.1124/molpharm.121.000315.
32. Kannan, N., Haste, N., Taylor, S. S. & Neuwald, A. F. (2007). The hallmark of AGC kinase functional divergence is its C-terminal tail, a cis-acting regulatory module. Proc Natl Acad Sci U S A. **104**, 1272-1277. https://doi.org/10.1073/pnas.0610251104.

33. McCusker, D., Denison, C., Anderson, S., Egelhofer, T. A., Yates, J. R., 3rd, Gygi, S. P. & Kellogg, D. R. (2007). Cdk1 coordinates cell-surface growth with the cell cycle. Nat Cell Biol. **9**, 506-515. https://doi.org/10.1038/ncb1568.
34. Koivomagi, M., Swaffer, M. P., Turner, J. J., Marinov, G. & Skotheim, J. M. (2021). G1 cyclin-Cdk promotes cell cycle entry through localized phosphorylation of RNA polymerase II. Science. **374**, 347-351. https://doi.org/10.1126/science.aba5186.
35. Liu, Y. L., Jang, H., Zhang, M. Z., Tsai, C. J., Maloney, R. & Nussinov, R. (2022). The structural basis of BCR-ABL recruitment of GRB2 in chronic myelogenous leukemia. Biophysical Journal. **121**, 2251-2265. https://doi.org/10.1016/j.bpj.2022.05.030.
36. Liu, Y., Zhang, M., Tsai, C. J., Jang, H. & Nussinov, R. (2022). Allosteric regulation of autoinhibition and activation of c-Abl. Comput Struct Biotechnol J. **20**, 4257-4270. https://doi.org/10.1016/j.csbj.2022.08.014.
37. Zhang, M. Z., Maloney, R., Jang, H. & Nussinov, R. (2021). The mechanism of Raf activation through dimerization. Chem Sci. **12**, 15609-15619. https://doi.org/10.1039/d1sc03444h.
38. Jang, H., Smith, I. N., Eng, C. & Nussinov, R. (2021). The mechanism of full activation of tumor suppressor PTEN at the phosphoinositide-enriched membrane. iScience. **24**, 102438. https://doi.org/10.1016/j.isci.2021.102438.
39. Jang, H., Zhang, M. Z. & Nussinov, R. (2020). The quaternary assembly of KRas4B with Raf-1 at the membrane. Comput Struct Biotec. **18**, 737-748. https://doi.org/10.1016/j.csbj.2020.03.018.
40. Zhang, W., Liu, Y., Jang, H. & Nussinov, R. (2023). Cell cycle progression mechanisms: slower cyclin-D/CDK4 activation and faster cyclin-E/CDK2. bioRxiv. https://doi.org/10.1101/2023.08.16.553605.
41. Jang, H., Banerjee, A., Marcus, K., Makowski, L., Mattos, C., Gaponenko, V. & Nussinov, R. (2019). The Structural Basis of the Farnesylated and Methylated KRas4B Interaction with Calmodulin. Structure. **27**, 1647-+. https://doi.org/10.1016/j.str.2019.08.009.
42. Brooks, B. R., Brooks, C. L., Mackerell, A. D., Nilsson, L., Petrella, R. J., Roux, B., Won, Y., Archontis, G., Bartels, C., Boresch, S., Caflisch, A., Caves, L., Cui, Q., Dinner, A. R., Feig, M., Fischer, S., Gao, J., Hodoscek, M., Im, W., Kuczera, K., Lazaridis, T., Ma, J., Ovchinnikov, V., Paci, E., Pastor, R. W., Post, C. B., Pu, J. Z., Schaefer, M., Tidor, B., Venable, R. M., Woodcock, H. L., Wu, X., Yang, W., York, D. M. & Karplus, M. (2009). CHARMM: The Biomolecular Simulation Program. J Comput Chem. **30**, 1545-1614. https://doi.org/10.1002/jcc.21287.
43. Huang, J., Rauscher, S., Nawrocki, G., Ran, T., Feig, M., de Groot, B. L., Grubmuller, H. & MacKerell, A. D. (2017). CHARMM36m: an improved force field for folded and intrinsically disordered proteins. Nat Methods. **14**, 71-73. https://doi.org/10.1038/Nmeth.4067.
44. Klauda, J. B., Venable, R. M., Freites, J. A., O'Connor, J. W., Tobias, D. J., Mondragon-Ramirez, C., Vorobyov, I., MacKerell, A. D., Jr. & Pastor, R. W. (2010). Update of the CHARMM all-atom additive force field for lipids: validation on six lipid types. J Phys Chem B. **114**, 7830-7843. https://doi.org/10.1021/jp101759q.
45. Eastman, P., Galvelis, R., Peláez, R. P., Abreu, C. R. A., Farr, S. E., Gallicchio, E., Gorenko, A., Henry, M. M., Hu, F., Huang, J., Krämer, A., Michel, J., Mitchell, J. A., Pande, V. S., Rodrigues, J. P., Rodriguez-Guerra, J., Simmonett, A. C., Singh, S., Swails, J., Turner, P., Wang, Y., Zhang, I., Chodera, J. D., De Fabritiis, G. & Markland, T. E. (2023). OpenMM 8: Molecular Dynamics Simulation with Machine Learning Potentials. The Journal of Physical Chemistry B. **128**, 109-116. https://doi.org/10.1021/acs.jpcb.3c06662.
46. Gentleman, R., Eastman, P., Swails, J., Chodera, J. D., McGibbon, R. T., Zhao, Y., Beauchamp, K. A., Wang, L.-P., Simmonett, A. C., Harrigan, M. P., Stern, C. D., Wiewiora, R. P., Brooks, B. R. & Pande, V. S. (2017). OpenMM 7: Rapid development of high performance algorithms for molecular dynamics. Plos Comput Biol. **13**. https://doi.org/10.1371/journal.pcbi.1005659.
47. Michaud-Agrawal, N., Denning, E. J., Woolf, T. B. & Beckstein, O. (2011). MDAnalysis: a toolkit for the analysis of molecular dynamics simulations. J Comput Chem. **32**, 2319-2327. https://doi.org/10.1002/jcc.21787.
48. McGibbon, Robert T., Beauchamp, Kyle A., Harrigan, Matthew P., Klein, C., Swails, Jason M., Hernández, Carlos X., Schwantes, Christian R., Wang, L.-P., Lane, Thomas J. & Pande, Vijay S. (2015). MDTraj: A

Modern Open Library for the Analysis of Molecular Dynamics Trajectories. Biophysical Journal. **109**, 1528-1532. https://doi.org/10.1016/j.bpj.2015.08.015.

49. Grant, B. J., Rodrigues, A. P. C., ElSawy, K. M., McCammon, J. A. & Caves, L. S. D. (2006). Bio3d: an R package for the comparative analysis of protein structures. Bioinformatics. **22**, 2695-2696. https://doi.org/10.1093/bioinformatics/btl461.
50. Team, R. C. (2013). R: A language and environment for statistical computing. Foundation for Statistical Computing.
51. Case, D. A., Aktulga, H. M., Belfon, K., Cerutti, D. S., Cisneros, G. A., Cruzeiro, V. W. D., Forouzesh, N., Giese, T. J., Götz, A. W., Gohlke, H., Izadi, S., Kasavajhala, K., Kaymak, M. C., King, E., Kurtzman, T., Lee, T.-S., Li, P., Liu, J., Luchko, T., Luo, R., Manathunga, M., Machado, M. R., Nguyen, H. M., O'Hearn, K. A., Onufriev, A. V., Pan, F., Pantano, S., Qi, R., Rahnamoun, A., Risheh, A., Schott-Verdugo, S., Shajan, A., Swails, J., Wang, J., Wei, H., Wu, X., Wu, Y., Zhang, S., Zhao, S., Zhu, Q., Cheatham, T. E., Roe, D. R., Roitberg, A., Simmerling, C., York, D. M., Nagan, M. C. & Merz, K. M. (2023). AmberTools. Journal of Chemical Information and Modeling. **63**, 6183-6191. https://doi.org/10.1021/acs.jcim.3c01153.
52. Van Wart, A. T., Durrant, J., Votapka, L. & Amaro, R. E. (2014). Weighted Implementation of Suboptimal Paths (WISP): An Optimized Algorithm and Tool for Dynamical Network Analysis. J Chem Theory Comput. **10**, 511-517. https://doi.org/10.1021/ct4008603.
53. Humphrey, W., Dalke, A. & Schulten, K. (1996). VMD: Visual molecular dynamics. J Mol Graph Model. **14**, 33-38. https://doi.org/Doi 10.1016/0263-7855(96)00018-5.
54. DeLano, W. L. (2002). The PyMOL Molecular Graphics System. Delano Scientific.
55. Wood, D. J. & Endicott, J. A. (2018). Structural insights into the functional diversity of the CDK-cyclin family. Open Biol. **8**. https://doi.org/10.1098/rsob.180112.
56. Arter, C., Trask, L., Ward, S., Yeoh, S. & Bayliss, R. (2022). Structural features of the protein kinase domain and targeted binding by small-molecule inhibitors. J Biol Chem. **298**. https://doi.org/10.1016/j.jbc.2022.102247.
57. Foster, S. A., Whalen, D. M., Ozen, A., Wongchenko, M. J., Yin, J., Yen, I., Schaefer, G., Mayfield, J. D., Chmielecki, J., Stephens, P. J., Albacker, L. A., Yan, Y., Song, K., Hatzivassiliou, G., Eigenbrot, C., Yu, C., Shaw, A. S., Manning, G., Skelton, N. J., Hymowitz, S. G. & Malek, S. (2016). Activation Mechanism of Oncogenic Deletion Mutations in BRAF, EGFR, and HER2. Cancer Cell. **29**, 477-493. https://doi.org/10.1016/j.ccell.2016.02.010.
58. Nussinov, R., Liu, Y., Zhang, W. & Jang, H. (2023). Protein conformational ensembles in function: roles and mechanisms. RSC Chemical Biology. https://doi.org/10.1039/d3cb00114h.
59. Nussinov, R., Liu, Y., Zhang, W. & Jang, H. (2023). Cell phenotypes can be predicted from propensities of protein conformations. Curr Opin Struct Biol. **83**, 102722. https://doi.org/10.1016/j.sbi.2023.102722.
60. Adon, T., Shanmugarajan, D. & Kumar, H. Y. (2021). CDK4/6 inhibitors: a brief overview and prospective research directions. RSC Advances. **11**, 29227-29246. https://doi.org/10.1039/d1ra03820f.
61. Guiley, K. Z., Stevenson, J. W., Lou, K., Barkovich, K. J., Kumarasamy, V., Wijeratne, T. U., Bunch, K. L., Tripathi, S., Knudsen, E. S., Witkiewicz, A. K., Shokat, K. M. & Rubin, S. M. (2019). p27 allosterically activates cyclin-dependent kinase 4 and antagonizes palbociclib inhibition. Science. **366**. https://doi.org/10.1126/science.aaw2106.
62. Frederick, K. K., Marlow, M. S., Valentine, K. G. & Wand, A. J. (2007). Conformational entropy in molecular recognition by proteins. Nature. **448**, 325-329. https://doi.org/10.1038/nature05959.
63. Ahuja, L. G., Aoto, P. C., Kornev, A. P., Veglia, G. & Taylor, S. S. (2019). Dynamic allostery-based molecular workings of kinase:peptide complexes. Proc Natl Acad Sci U S A. **116**, 15052-15061. https://doi.org/10.1073/pnas.1900163116.
64. Kornev, A. P. & Taylor, S. S. (2015). Dynamics-Driven Allostery in Protein Kinases. Trends Biochem Sci. **40**, 628-647. https://doi.org/10.1016/j.tibs.2015.09.002.
65. Taylor, S. S., Wu, J., Bruystens, J. G. H., Del Rio, J. C., Lu, T. W., Kornev, A. P. & Ten Eyck, L. F. (2021). From structure to the dynamic regulation of a molecular switch: A journey over 3 decades. J Biol Chem. **296**, 100746. https://doi.org/10.1016/j.jbc.2021.100746.

66. Dixit, A. & Verkhivker, G. M. (2011). Computational modeling of allosteric communication reveals organizing principles of mutation-induced signaling in ABL and EGFR kinases. Plos Comput Biol. **7**, e1002179. https://doi.org/10.1371/journal.pcbi.1002179.
67. Meharena, H. S., Fan, X., Ahuja, L. G., Keshwani, M. M., McClendon, C. L., Chen, A. M., Adams, J. A. & Taylor, S. S. (2016). Decoding the Interactions Regulating the Active State Mechanics of Eukaryotic Protein Kinases. PLoS Biol. **14**, e2000127. https://doi.org/10.1371/journal.pbio.2000127.
68. Anders, L. & Gallego, G. (2024). Abstract ND12: Discovery of PF-07220060, a potent and selective CDK4 inhibitor. Cancer Res. **84**, ND12-ND12. https://doi.org/10.1158/1538-7445.Am2024-nd12.
69. McClendon, C. L., Kornev, A. P., Gilson, M. K. & Taylora, S. S. (2014). Dynamic architecture of a protein kinase. P Natl Acad Sci USA. **111**, E4623-E4631. https://doi.org/10.1073/pnas.1418402111.
70. Knight, Z. A. & Shokat, K. M. (2005). Features of selective kinase inhibitors. Chem Biol. **12**, 621-637. https://doi.org/10.1016/j.chembiol.2005.04.011.
71. Schonherr, H., Ayaz, P., Taylor, A. M., Casaletto, J. B., Toure, B. B., Moustakas, D. T., Hudson, B. M., Valverde, R., Zhao, S., O'Hearn, P. J., Foster, L., Sharon, D. A., Garfinkle, S., Giordanetto, F., Lescarbeau, A., Kurukulasuriya, R., Gerami-Moayed, N., Maglic, D., Bruderek, K., Naik, G., Gunaydin, H., Mader, M. M., Boezio, A. A., McLean, T. H., Chen, R., Wang, Y., Shaw, D. E., Watters, J. & Bergstrom, D. A. (2024). Discovery of lirafugratinib (RLY-4008), a highly selective irreversible small-molecule inhibitor of FGFR2. Proc Natl Acad Sci U S A. **121**, e2317756121. https://doi.org/10.1073/pnas.2317756121.
72. Hinz, N. & Jucker, M. (2019). Distinct functions of AKT isoforms in breast cancer: a comprehensive review. Cell Commun Signal. **17**, 154. https://doi.org/10.1186/s12964-019-0450-3.
73. Chu, N., Salguero, A. L., Liu, A. Z., Chen, Z., Dempsey, D. R., Ficarro, S. B., Alexander, W. M., Marto, J. A., Li, Y., Amzel, L. M., Gabelli, S. B. & Cole, P. A. (2018). Akt Kinase Activation Mechanisms Revealed Using Protein Semisynthesis. Cell. **174**, 897-907 e814. https://doi.org/10.1016/j.cell.2018.07.003.
74. Kargbo, R. B. (2023). Targeted Degradation of CDK4/6: An Innovative Approach to Overcoming Cancer Drug Resistance. ACS Med Chem Lett. **14**, 1162-1164. https://doi.org/10.1021/acsmedchemlett.3c00356.

Graphical abstract

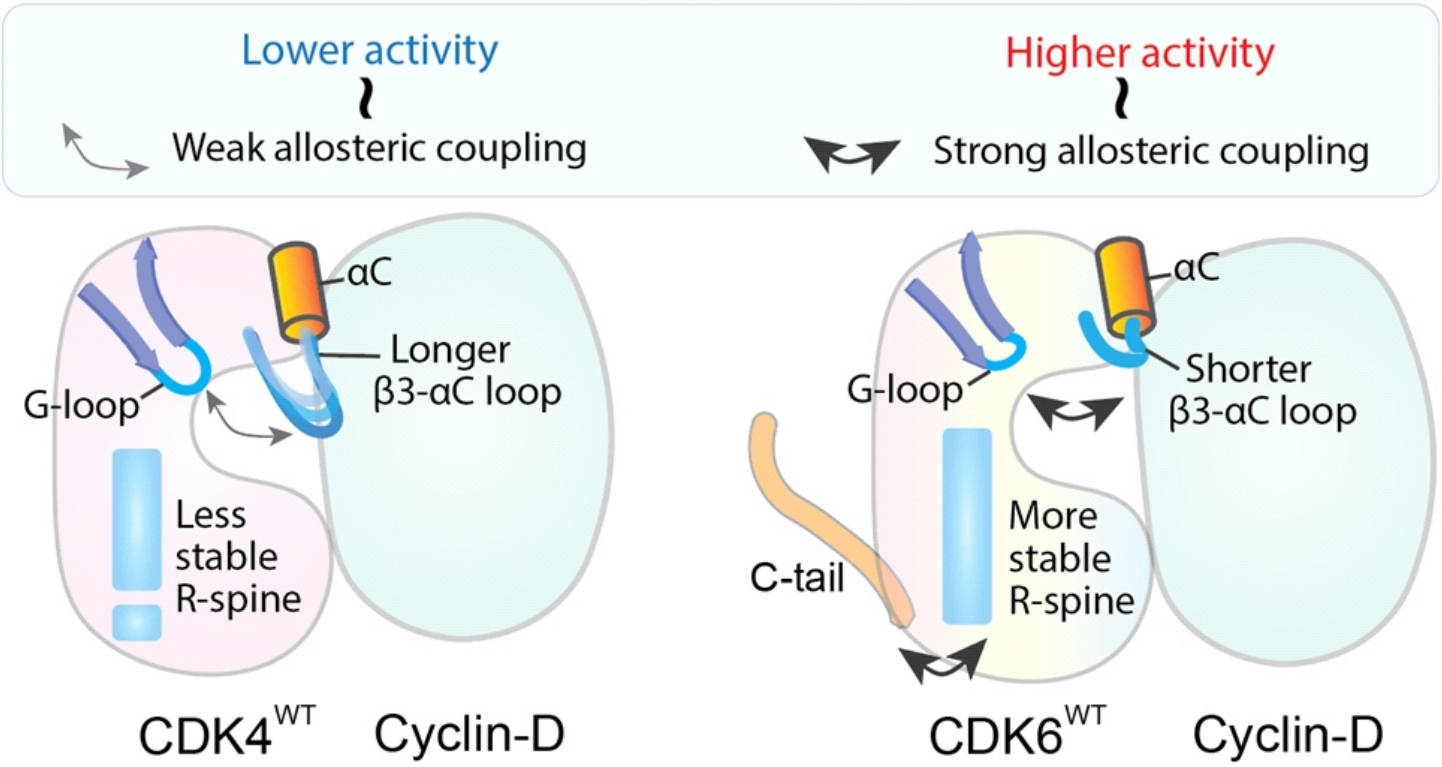

# Figure 1

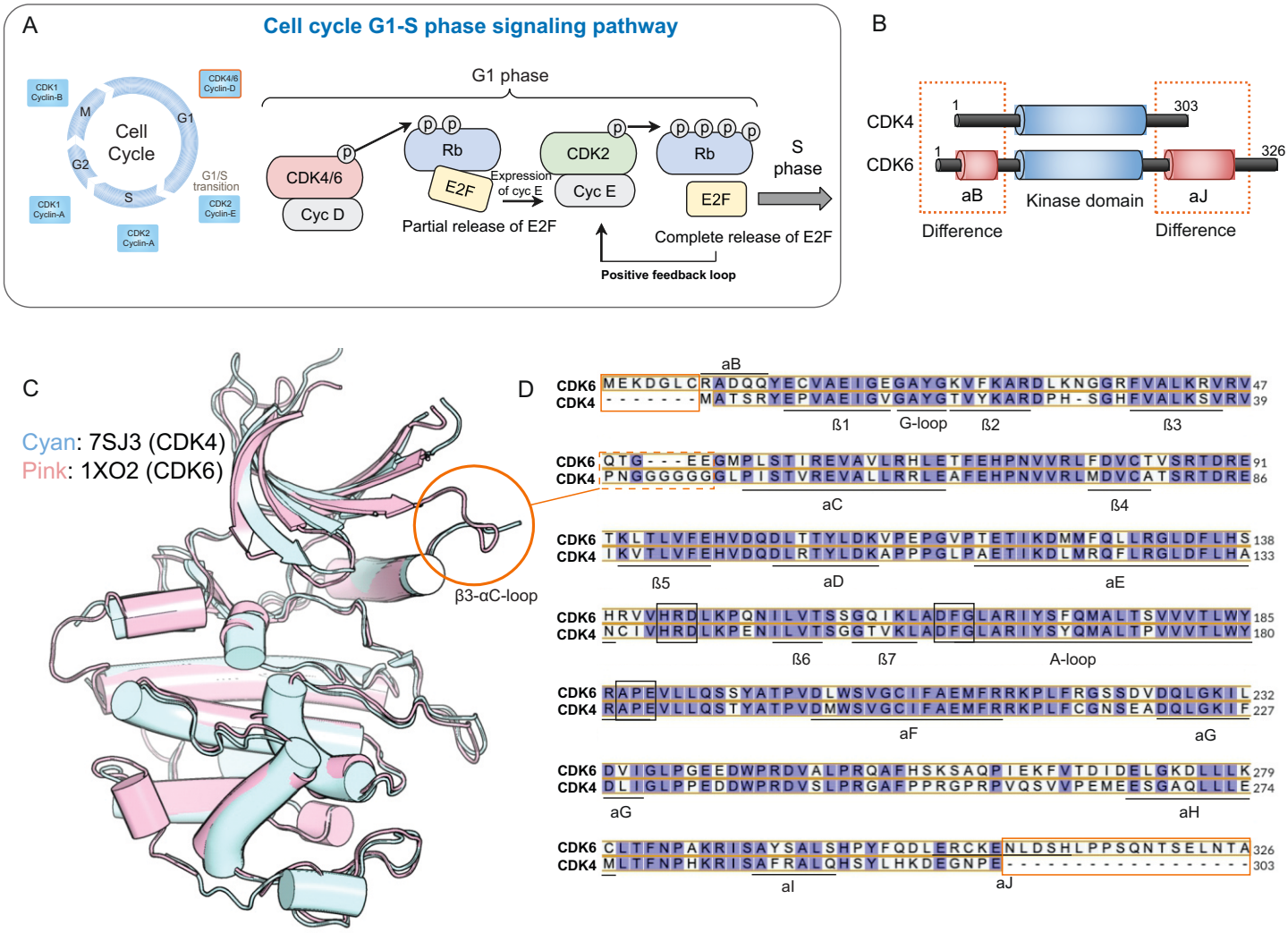
A
Cell cycle G1-S phase signaling pathway
CDK1 Cyclin-B
CDK4/6 Cyclin-D
M
G1
Cell Cycle
G2
S
G1/S transition
CDK1 Cyclin-A
CDK2 Cyclin-E
CDK2 Cyclin-A
G1 phase
CDK4/6
Cyc D
Rb
E2F
Expression of cyc E
Partial release of E2F
CDK2
Cyc E
Rb
E2F
S phase
Complete release of E2F
Positive feedback loop
B
CDK4
CDK6
1
303
1
326
aB
Kinase domain
aJ
Difference
Difference
C
Cyan: 7SJ3 (CDK4)
Pink: 1XO2 (CDK6)
β3-αC-loop
D
aB
CDK6 MEKDGLCRADQQYECVAEIGEGAYGKVFKARDLKNGGRFVALKRVRV 47
CDK4 -------MATSRYEPVAEIGVGAYGTVYKARDPH-SGHFVALKSVRV 39
ß1 G-loop ß2 ß3
CDK6 QTG---EEGMPLSTIREVAVLRHLETFEHPNVVRLFDVCTVSRTDRE 91
CDK4 PNGGGGGGGLPISTVREVALLRRLEAFEHPNVVRLMDVCATSRTDRE 86
aC ß4
CDK6 TKLTLVFEHVDQDLTTYLDKVPEPGVPTETIKDMMFQLLRGLDFLHS 138
CDK4 IKVTLVFEHVDQDLRTYLDKAPPPGLPAETIKDLMRQFLRGLDFLHA 133
ß5 aD aE
CDK6 HRVVHRDLKPQNILVTSSGQIKLADFGLARIYSFQMALTSVVVTLWY 185
CDK4 NCIVHRDLKPENILVTSGGTVKLADFGLARIYSYQMALTPVVVTLWY 180
ß6 ß7 A-loop
CDK6 RAPEVLLQSSYATPVDLWSVGCIFAEMFRRKPLFRGSSDVDQLGKIL 232
CDK4 RAPEVLLQSTYATPVDMWSVGCIFAEMFRRKPLFCGNSEADQLGKIF 227
aF aG
CDK6 DVIGLPGEEDWPRDVALPRQAFHSKSAQPIEKFVTDIDELGKDLLLK 279
CDK4 DLIGLPPEDDWPRDVSLPRGAFPPRGPRPVQSVVPEMEESGAQLLLE 274
aG aH
CDK6 CLTFNPAKRISAYSALSHPYFQDLERCKENLDSHLPPSQNTSELNTA 326
CDK4 MLTFNPHKRISAFRALQHSYLHKDEGNPE-----------------303
aI aJ

Figure 2

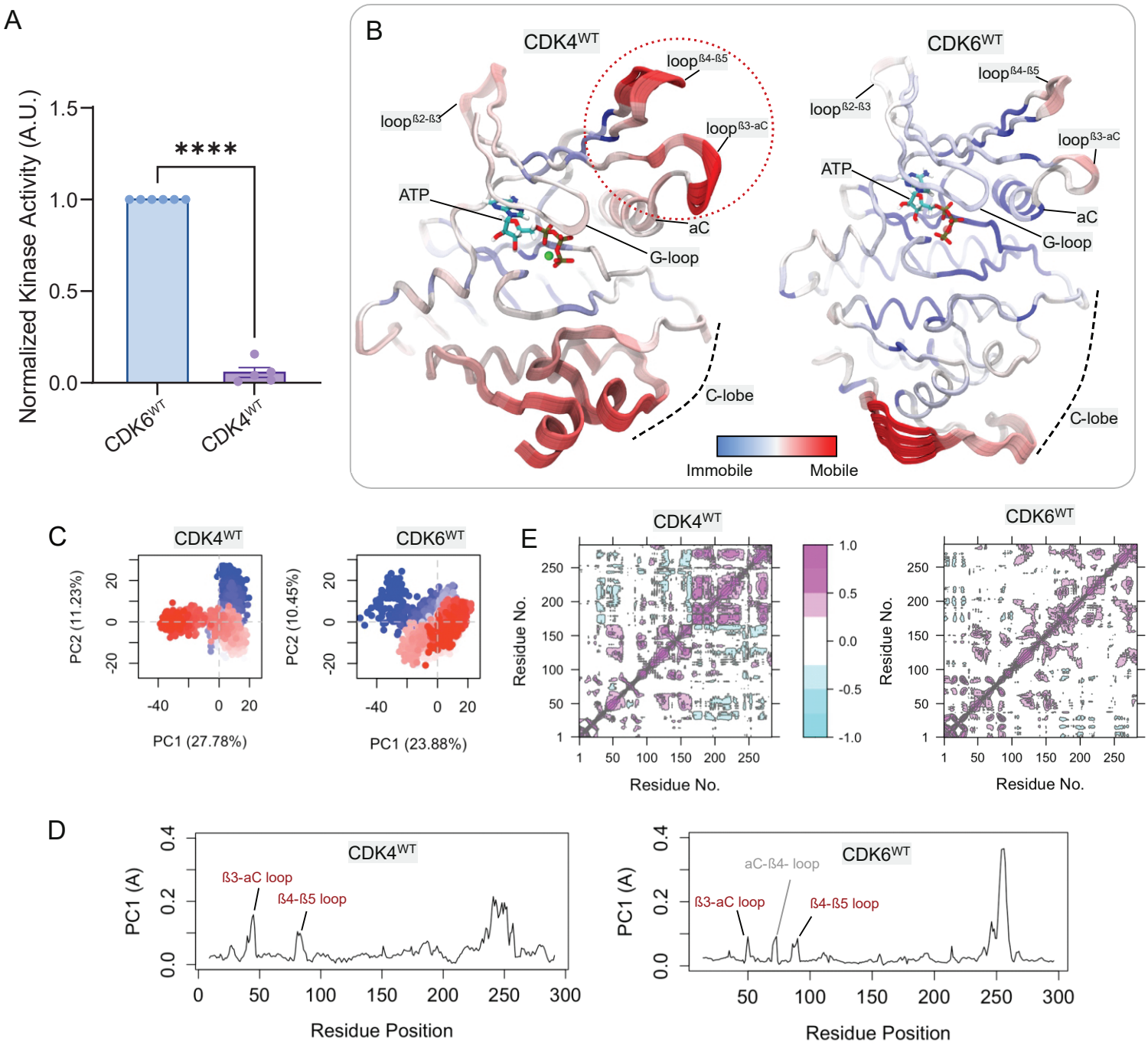
A
Normalized Kinase Activity (A.U.)
1.5
1.0
0.5
0.0
****
CDK6WT
CDK4WT
B
CDK4WT
CDK6WT
loopß2-ß3
loopß4-ß5
loopß3-aC
ATP
aC
G-loop
C-lobe
Immobile
Mobile
C
CDK4WT
CDK6WT
PC2 (11.23%)
PC1 (27.78%)
PC2 (10.45%)
PC1 (23.88%)
E
Residue No.
D
PC1 (A)
ß3-aC loop
ß4-ß5 loop
aC-ß4- loop
Residue Position

# Figure 3

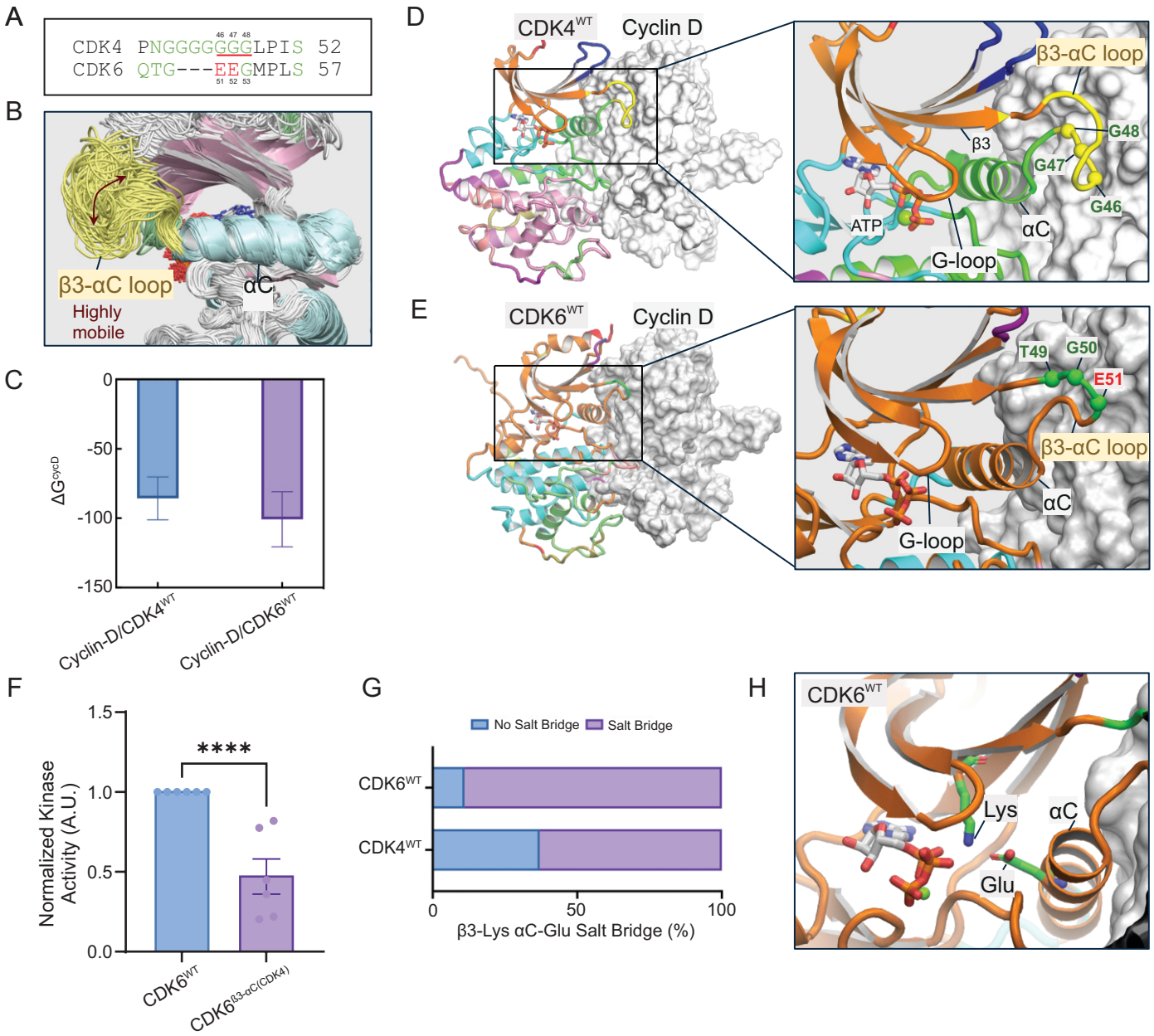
A
CDK4 PNGGGGGGGLPIS 52
CDK6 QTG---EEGMPLS 57
46 47 48
51 52 53
B
β3-αC loop
Highly mobile
αC
C
ΔG^cycD
0
-50
-100
-150
Cyclin-D/CDK4^WT
Cyclin-D/CDK6^WT
D
CDK4^WT
Cyclin D
β3-αC loop
β3
G48
G47
G46
ATP
αC
G-loop
E
CDK6^WT
Cyclin D
T49
G50
E51
β3-αC loop
αC
G-loop
F
Normalized Kinase Activity (A.U.)
1.5
1.0
0.5
0.0
****
CDK6^WT
CDK6^β3-αC(CDK4)
G
No Salt Bridge
Salt Bridge
CDK6^WT
CDK4^WT
0
50
100
β3-Lys αC-Glu Salt Bridge (%)
H
CDK6^WT
Lys
αC
Glu

# Figure 4

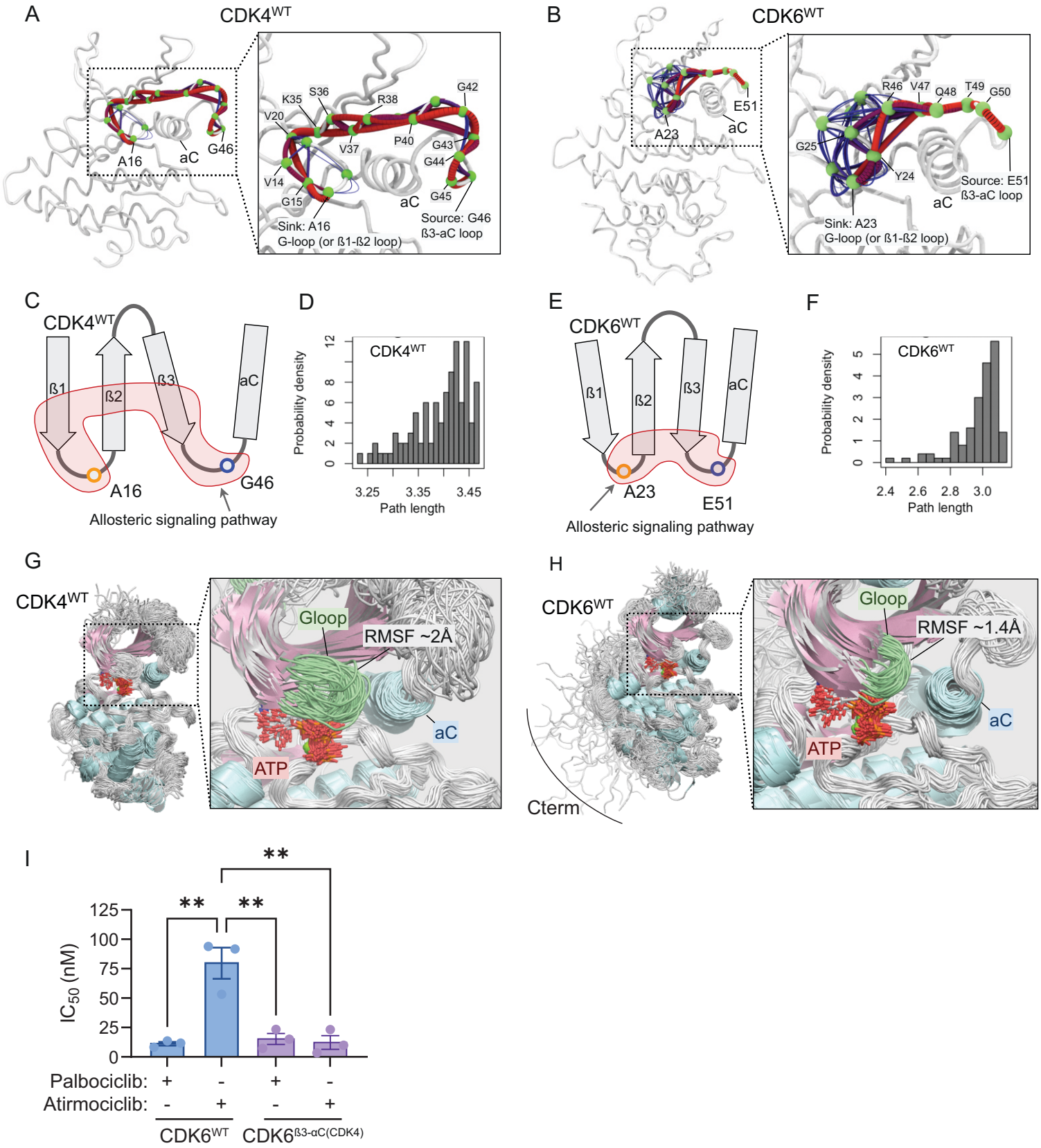
A
CDK4WT
A16
aC
G46
K35
S36
R38
G42
V20
V37
P40
G43
G44
V14
G15
aC
G45
Sink: A16
G-loop (or ß1-ß2 loop)
Source: G46
ß3-aC loop
B
CDK6WT
E51
aC
A23
R46
V47
Q48
T49
G50
G25
Y24
Source: E51
ß3-aC loop
aC
Sink: A23
G-loop (or ß1-ß2 loop)
C
CDK4WT
ß1
ß2
ß3
aC
A16
G46
Allosteric signaling pathway
D
CDK4WT
Probability density
Path length
E
CDK6WT
ß1
ß2
ß3
aC
A23
E51
Allosteric signaling pathway
F
CDK6WT
Probability density
Path length
G
CDK4WT
Gloop
RMSF ~2Å
aC
ATP
H
CDK6WT
Gloop
RMSF ~1.4Å
aC
ATP
Cterm
I
IC50 (nM)
Palbociclib:
Atirmociclib:
CDK6WT
CDK6ß3-αC(CDK4)

# Figure 5

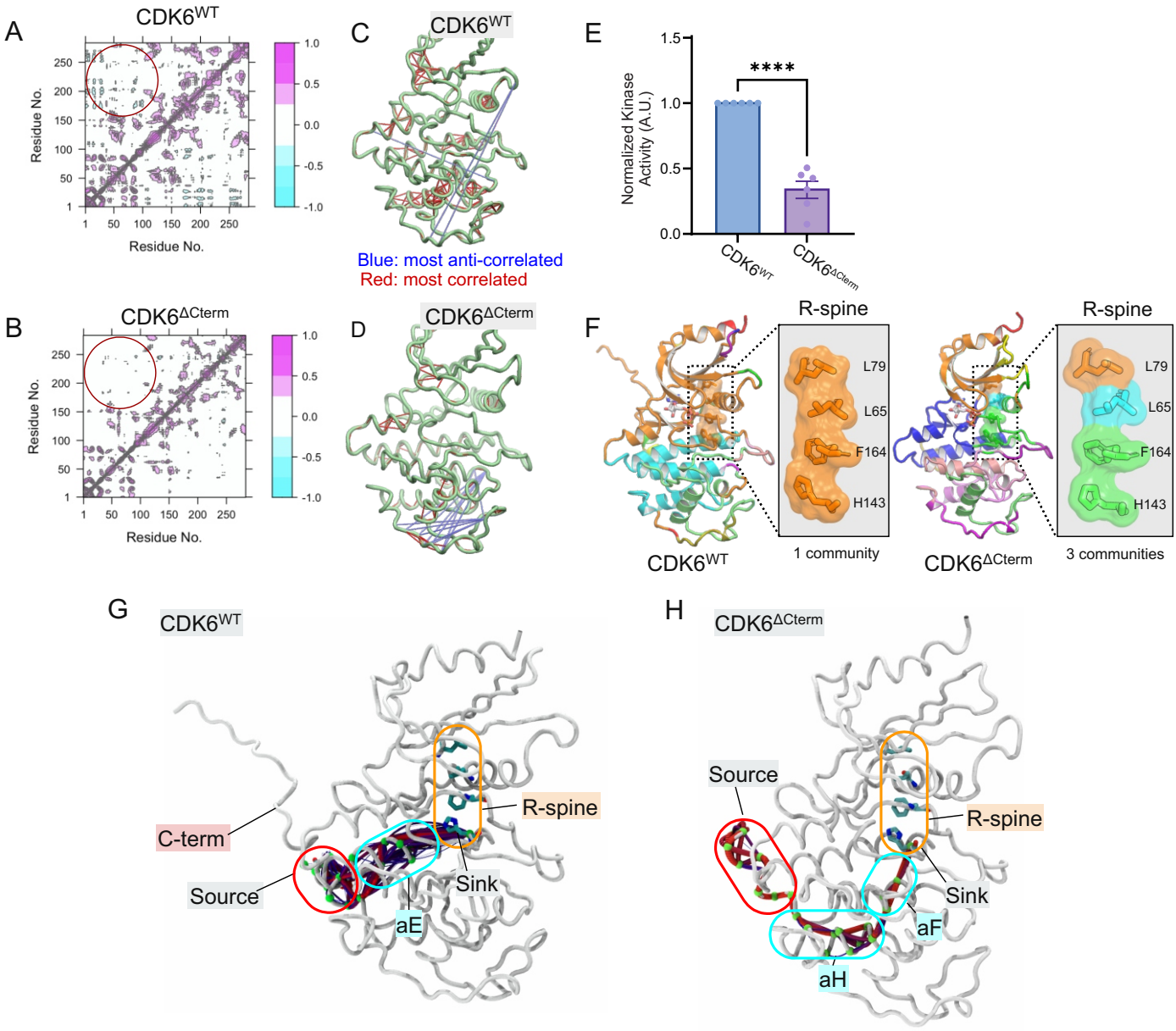
A
CDK6WT
Residue No.
Residue No.
B
CDK6ΔCterm
Residue No.
Residue No.
C
CDK6WT
Blue: most anti-correlated
Red: most correlated
D
CDK6ΔCterm
E
Normalized Kinase Activity (A.U.)
****
CDK6WT
CDK6ΔCterm
F
R-spine
L79
L65
F164
H143
CDK6WT
1 community
R-spine
L79
L65
F164
H143
CDK6ΔCterm
3 communities
G
CDK6WT
C-term
Source
R-spine
Sink
aE
H
CDK6ΔCterm
Source
R-spine
Sink
aF
aH

Figure 6

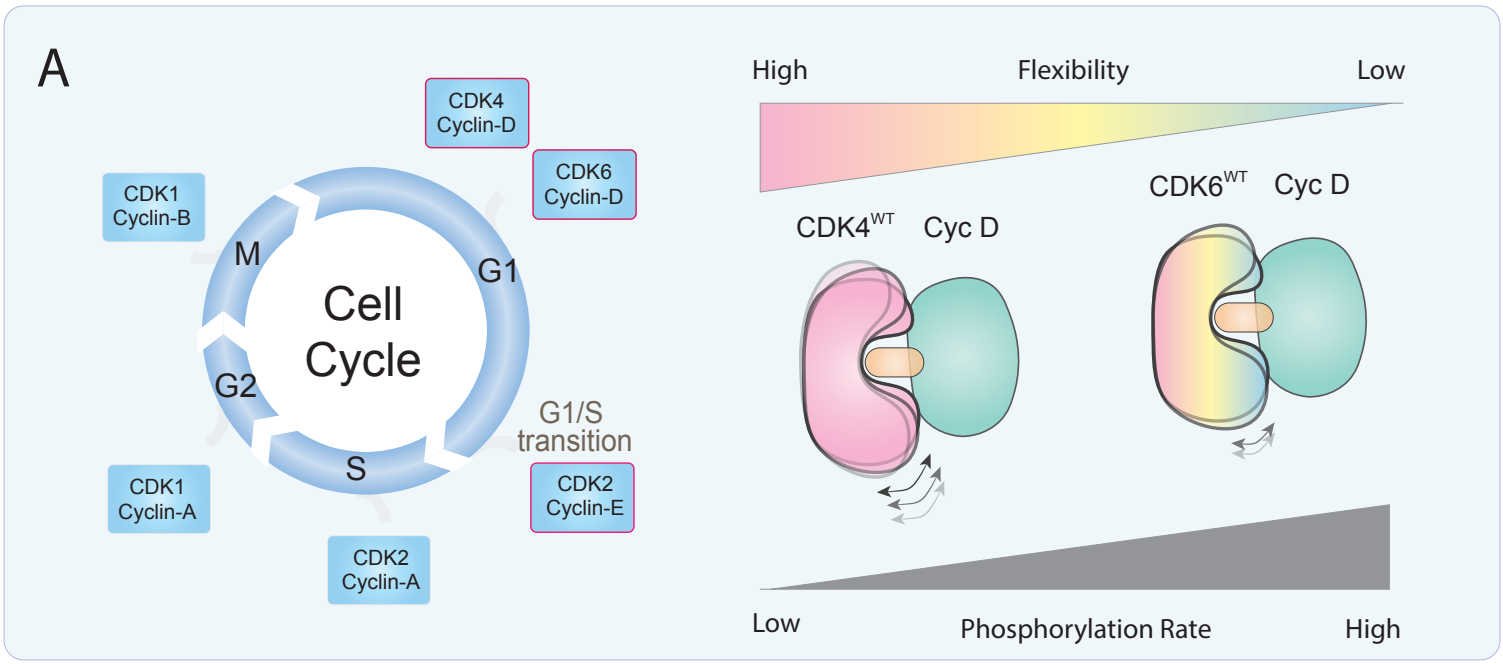
A
CDK4
Cyclin-D
CDK6
Cyclin-D
CDK1
Cyclin-B
M
G1
Cell
Cycle
G2
G1/S
transition
S
CDK1
Cyclin-A
CDK2
Cyclin-E
CDK2
Cyclin-A
High
Flexibility
Low
CDK4WT
Cyc D
CDK6WT
Cyc D
Low
Phosphorylation Rate
High

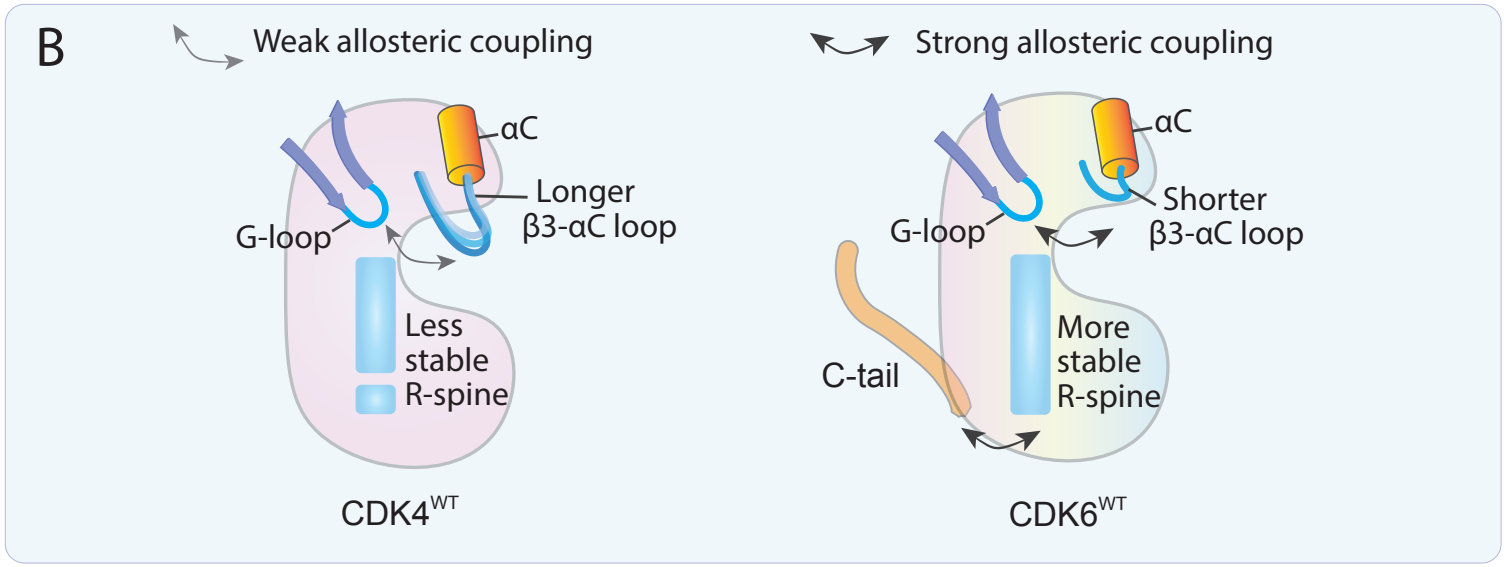
B
Weak allosteric coupling
Strong allosteric coupling
αC
Longer
β3-αC loop
G-loop
Less
stable
R-spine
CDK4WT
αC
Shorter
β3-αC loop
G-loop
C-tail
More
stable
R-spine
CDK6WT

# Supplementary Information:
# Distinct allosteric networks in CDK4 and CDK6 in the cell cycle and in drug resistance

Wengang Zhang,[1] Gretchen Heidebrink,[2] Devin Bradburn,[2] Yonglan Liu,[1] Hyunbum Jang,[1,3] and Ruth Nussinov[1,3,4*], Mardo Koivomagi[2, *]

[1]Cancer Innovation Laboratory, National Cancer Institute, Frederick, MD 21702, U.S.A.

[2]Laboratory of Biochemistry and Molecular Biology, National Cancer Institute, Bethesda, MD 20892, U.S.A.

[3]Computational Structural Biology Section, Frederick National Laboratory for Cancer Research, Frederick, MD 21702, U.S.A.

[4]Department of Human Molecular Genetics and Biochemistry, Sackler School of Medicine, Tel Aviv University, Tel Aviv 69978, Israel

* Author for correspondence: Mardo Koivomagi, Ruth Nussinov

**Email:** mardo.koivomagi@nih.gov NussinoR@mail.nih.gov

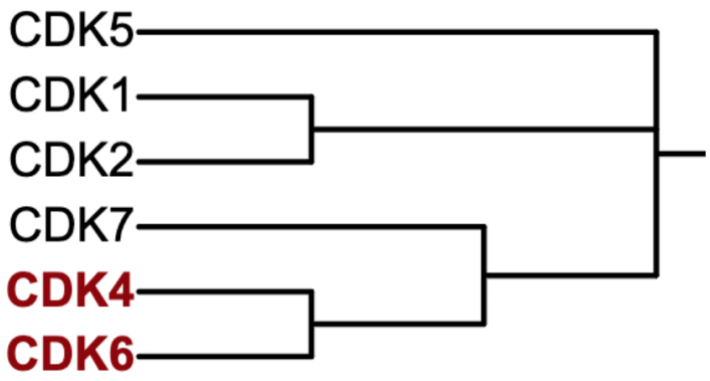

**Figure S1. Phylogenetic tree of human cell cycle CDKs.** It shows the evolutionary closeness of CDK4 and CDK6, compared to the rest of the cell cycle CDKs. The figure is visualized using [1].

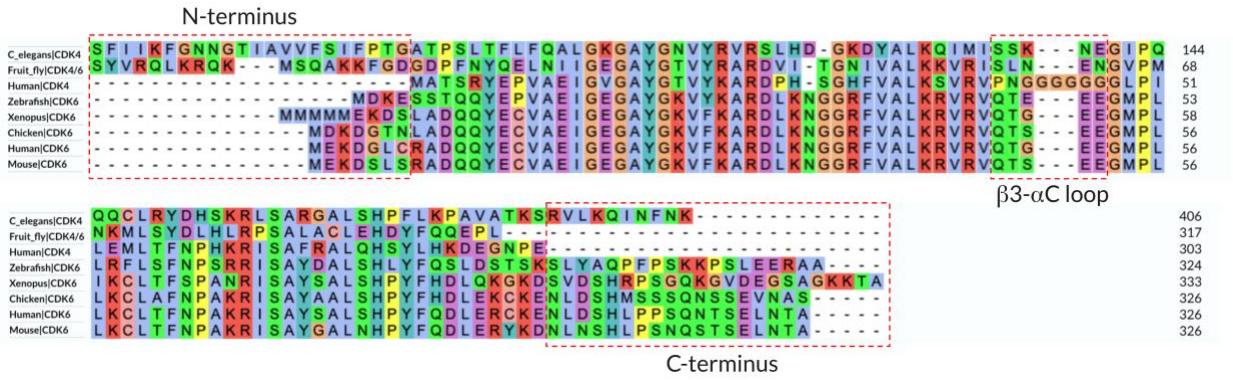


**Figure S2. Multi-species sequence alignment comparing the N- and C-terminal region and β3-αC loop across CDK 4 and CDK6**. The sequence divergence between human CDK4 and CDK6 is mostly conserved in other species as well. The alignment is colored by amino acid properties (red = positive charge, magenta= negative charge, blue = hydrophobic, green = polar, pink = cysteines, orange = glycines, yellow = prolines, cyan = aromatic) to highlight sequence conservation and variation. The key regions (N- and C-termini, and β3-αC loop) are highlighted in red boxes. Each row represents a CDK4 or CDK6 of species ortholog.

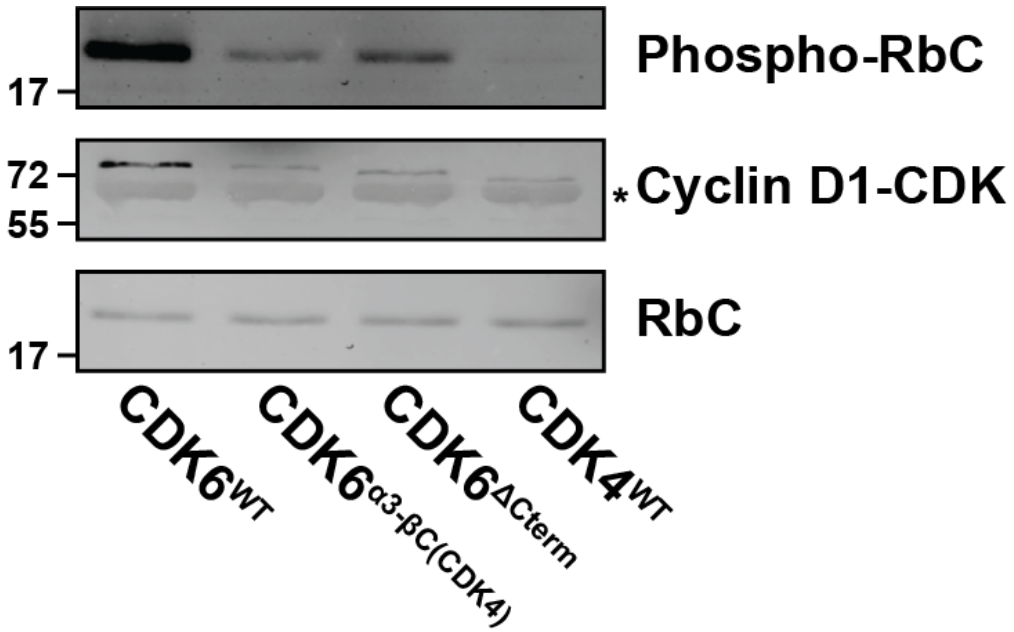


**Figure S3: Representative immunoblot of RbC phosphorylation by RbC.** *In vitro* phosphorylation of RbC by CDK6 (WT, β3-αC(CDK4), and ΔCterm) and CDK4 (WT). Shown is phosphorylated RbC (detected by anti-thiophosphate ester antibodies), cyclin D1-CDK fusions (detected by anti-FLAG antibodies), and RbC detected by total protein stain.

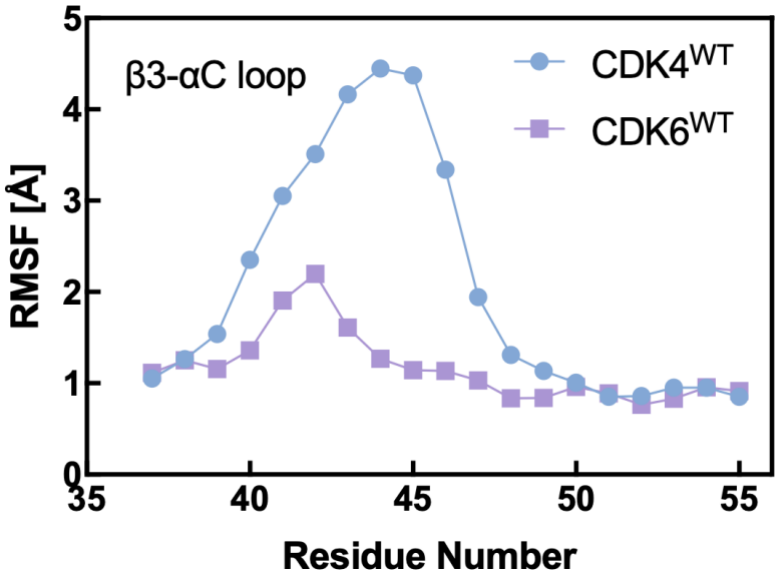


**Figure S4. Root mean square fluctuations (RMSFs) of β3-αC loop in CDK4$^{WT}$ and CDK6$^{WT}$.** The β3-αC loop in CDK4$^{WT}$ has significantly more fluctuation than that in CDK6$^{WT}$. Residue number for CDK6 is subtracted by 8 to match the β3-αC loop residues in CDK4.

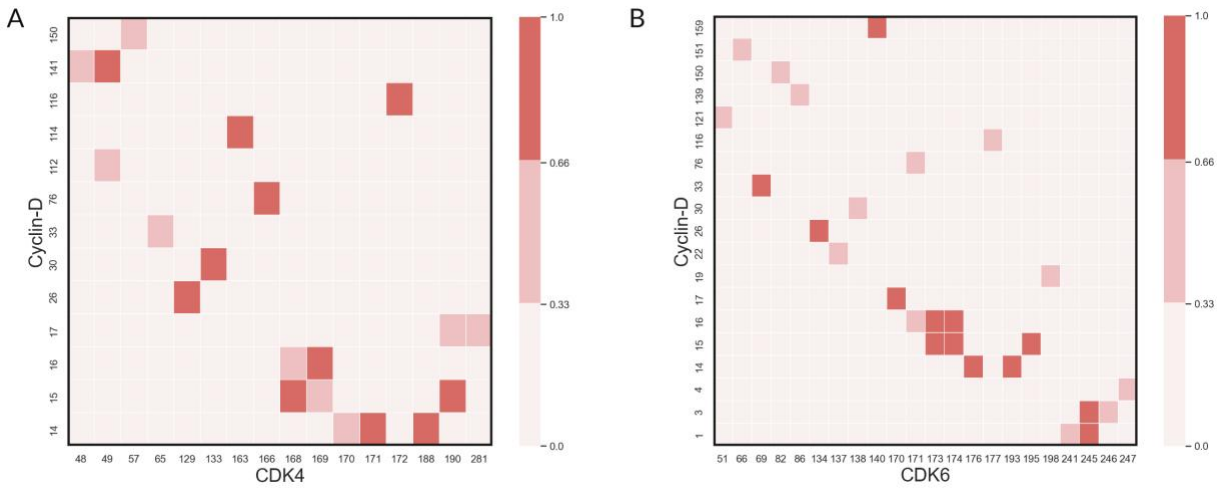


**Figure S5. Contacting residue map between CDK and cyclin for (A) cyclin-D/CDK4, and (B) cyclin-D/CDK6 complexes.** The x-axis represents residue numbers from CDK4/6, while the y-axis shows cyclin-D residues. The color intensity indicates contact frequency between residue pairs during the simulation, with darker red representing higher frequency contacts (scale from 0.0 to 1.0). These maps show more extensive contacting residues between CDK6 and cyclin-D, resulting in its stronger binding affinity.

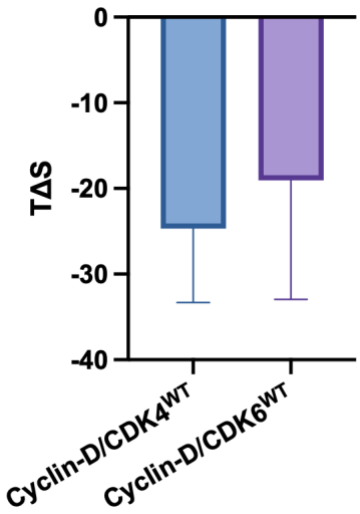


**Figure S6. Entropic contribution to the binding free energy between cyclin-D and either CDK4$^{WT}$ or CDK6$^{WT}$**. The higher degree of entropic contribution of CDK6 complex decreases its binding free energy with cyclin-D.

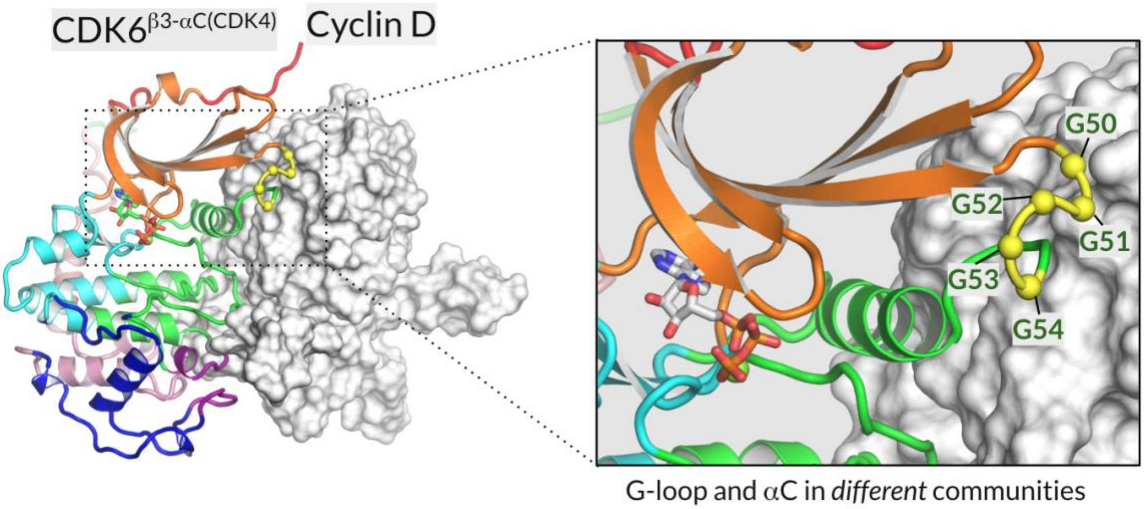


**Figure S7. Community analysis of CDK6$^{WT}$ and CDK6$^{\beta3\text{-}\alpha C(CDK4)}$.** It shows the impact of the longer CDK4 β3-αC loop can disrupt community organization breaking the coupling between β-strands in C-lobe and αC-helix in CDK6$^{WT}$ (**Fig. 3**). CDK6 is shown in cartoon representation with different colors representing distinct dynamic communities identified through community network analysis. Cyclin-D is displayed in surface representation (gray), highlighting the protein-protein interface. In the zoomed-in view of the G-loop and αC-helix, the G-loop residues (G50-G54) are highlighted in yellow against the cyclin-D surface (gray). The separation of the G-loop and αC-helix into different dynamic communities (shown by distinct colors: orange and green) demonstrates how incorporating the CDK4 β3-αC loop disrupts the normal coupling between these regulatory elements.

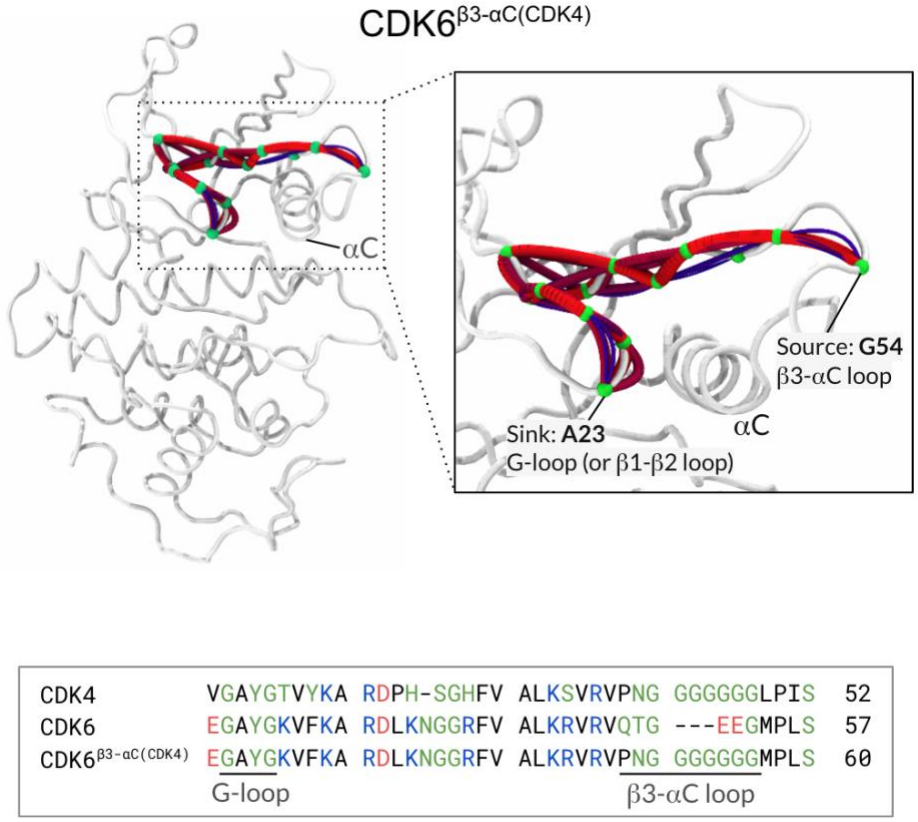


**Figure S8. Impact of β3-αC loop substitution on allosteric communication in CDK6$^{\beta3\text{-}\alpha C(CDK4)}$**. Structural visualization of allosteric pathways in CDK6$^{\beta3\text{-}\alpha C(CDK4)}$. CDK6$^{\beta3\text{-}\alpha C(CDK4)}$ is mutant of CDK6 with β3-αC loop swapped for that from CDK4. The zoomed-in view of the allosteric pathways between source residue A29 (in β3-αC loop) and G54 in the G-loop. It exhibits similar allosteric pathways compared to that of CDK4 in **Fig. 4**. Swapping β3-αC weaken the allosteric network between the β3-αC and G-loop, resulting in more dynamic G-loop (β1-β2 loop).

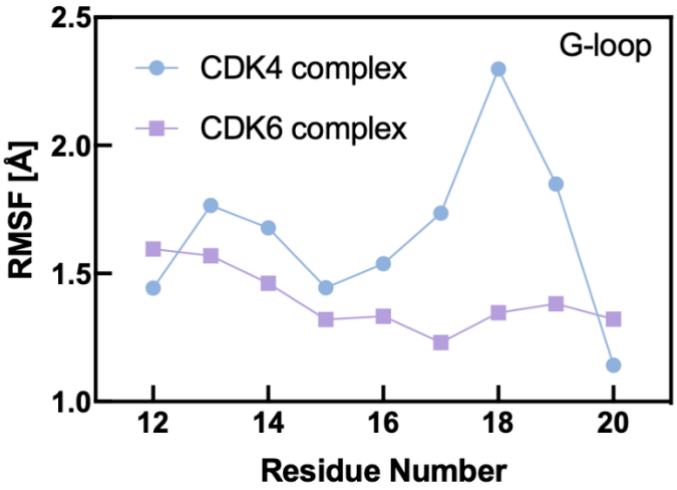


**Figure S9. Root mean square fluctuations (RMSFs) of G-loop in CDK4 and CDK6.** The G-loop of CDK4 has significantly more fluctuation than that in CDK6. The residue number for CDK6 is subtracted by 7 to match the G-loop residues in CDK4.

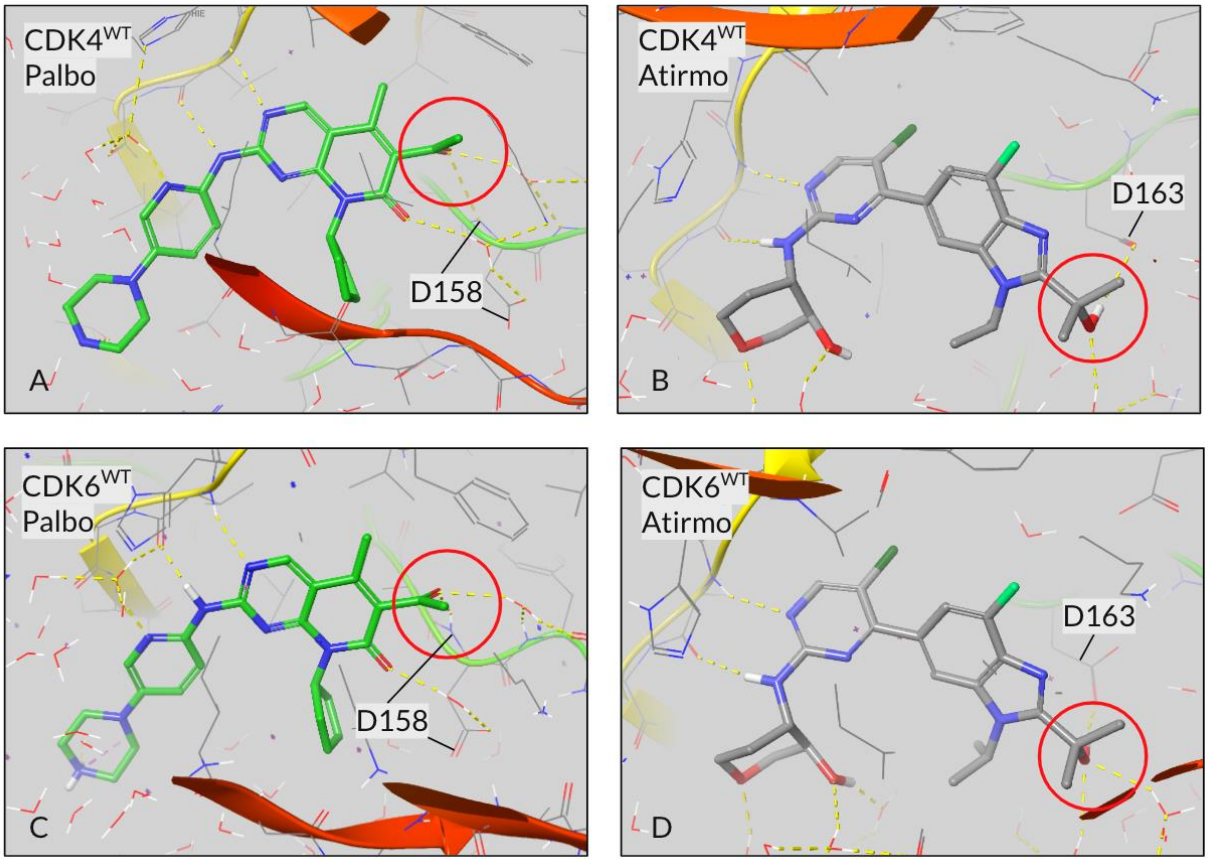


**Figure S10. Comparison of binding modes of palbociclib (PD 0332991) and atirmociclib (PF-07220060) in CDK4 and CDK6 active sites.** Both inhibitors interaction with the aspartic acid (D158 in CDK4, D163 in CDK6) in the DFG motif. (A) CDK4-palbociclib. (B) CDK4-atirmociclib. (C) CDK6-palbociclib. (D) CDK6-atirmociclib. Red circles highlight the carboxylic acid in palbocicilib and isopropyl alcohol in atirmociclib. The additional methyl group in isopropyl alcohol of atirmociclib is responsible for the selectivity of CDK4 due to the flexible G-loop right above this allowing for this bulkier group, in contrast to the less flexible G-loop in CDK6.

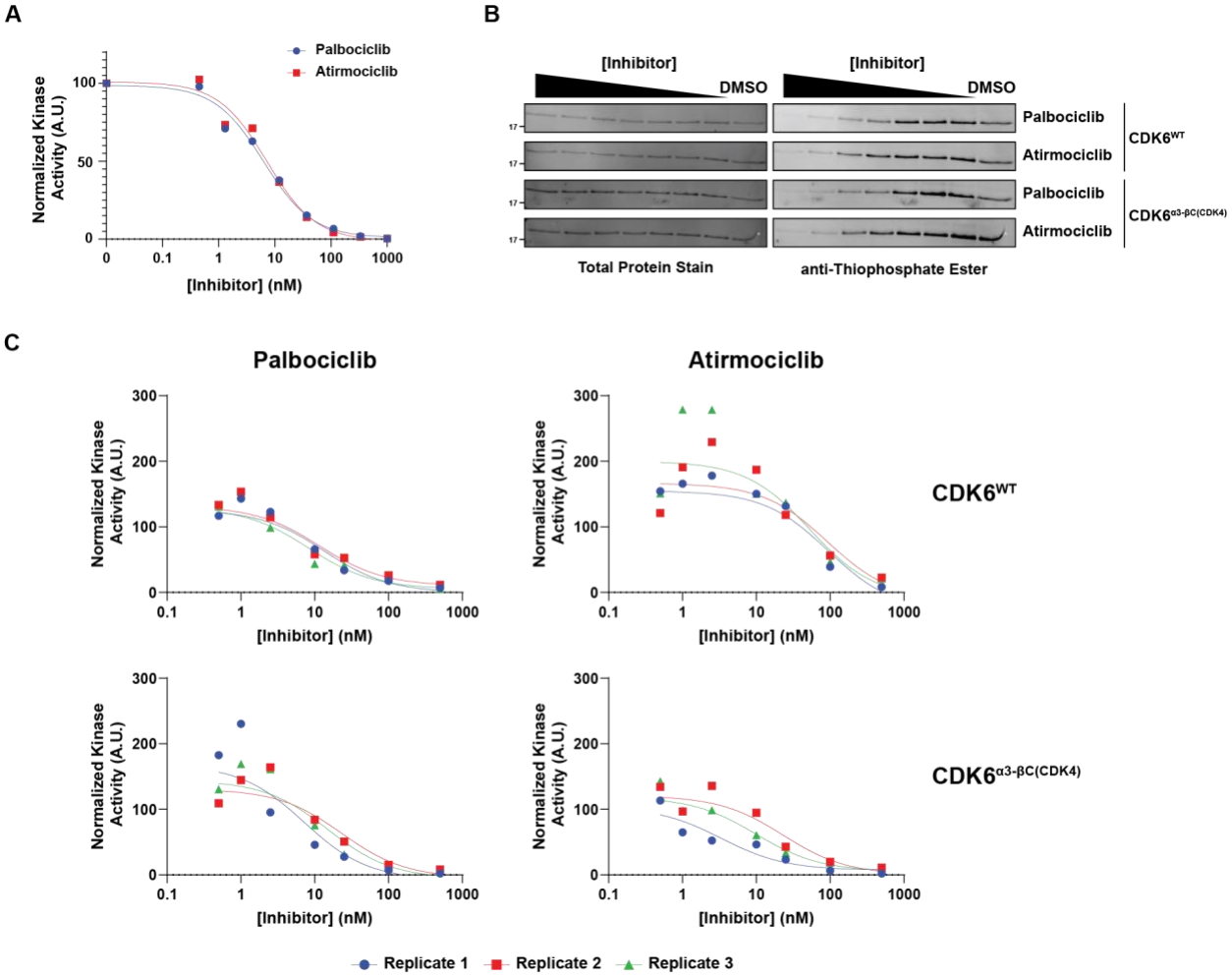


**Figure S11. *In vitro* CDK4/6 inhibition by palbociclib and atirmociclib.** (A) Palbociclib and atirmociclib mediated inhibition of CDK4 kinase activity toward RbC. (B) Representative immunoblot of palbociclib and atirmociclib mediated inhibition of $CDK6^{WT}$ and $CDK6^{\beta3\text{-}\alpha C(CDK4)}$ kinase activity toward RbC. (C) Individual inhibition curves used to calculate $IC_{50}$ values displayed in Fig. 4I.

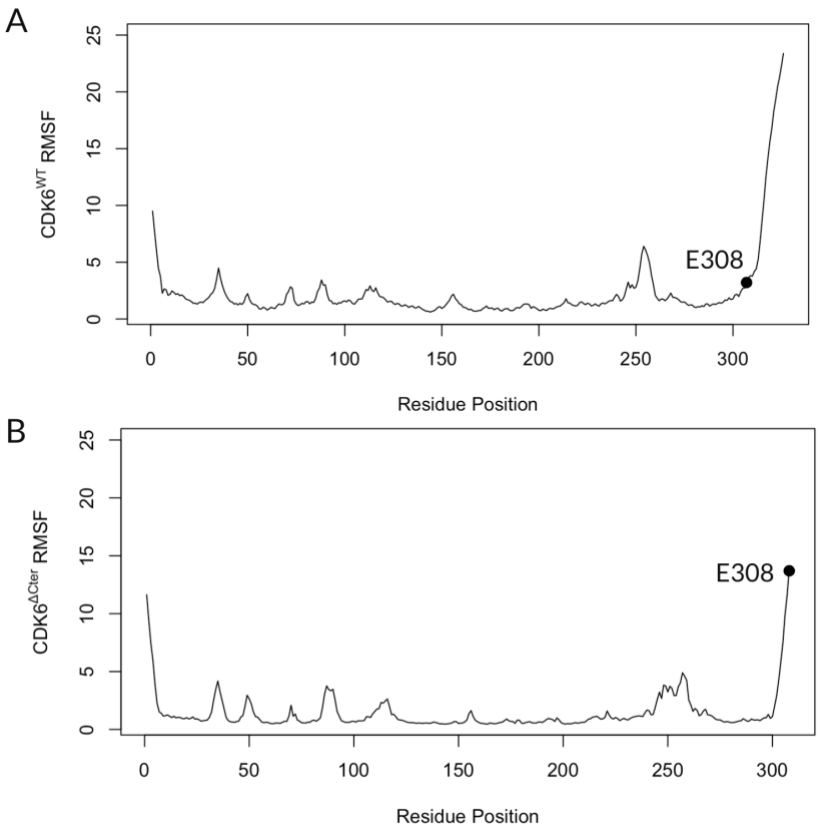


**Figure S12. Root mean square fluctuations (RMSFs) of CDK6$^{WT}$ and CDK6$^{\Delta Cterm}$.** E308, the last residue in CDK6$^{\Delta Cterm}$ has significantly more fluctuation than the same residue in CDK6$^{WT}$. The truncation of C-terminus results in an enhanced fluctuation in the last a few residues in the C-lobe, which leads to the disruption of the intrinsics dynamics of the kinase. For CDK6$^{WT}$, the longer C-terminus shielded E308 from significant fluctuation.

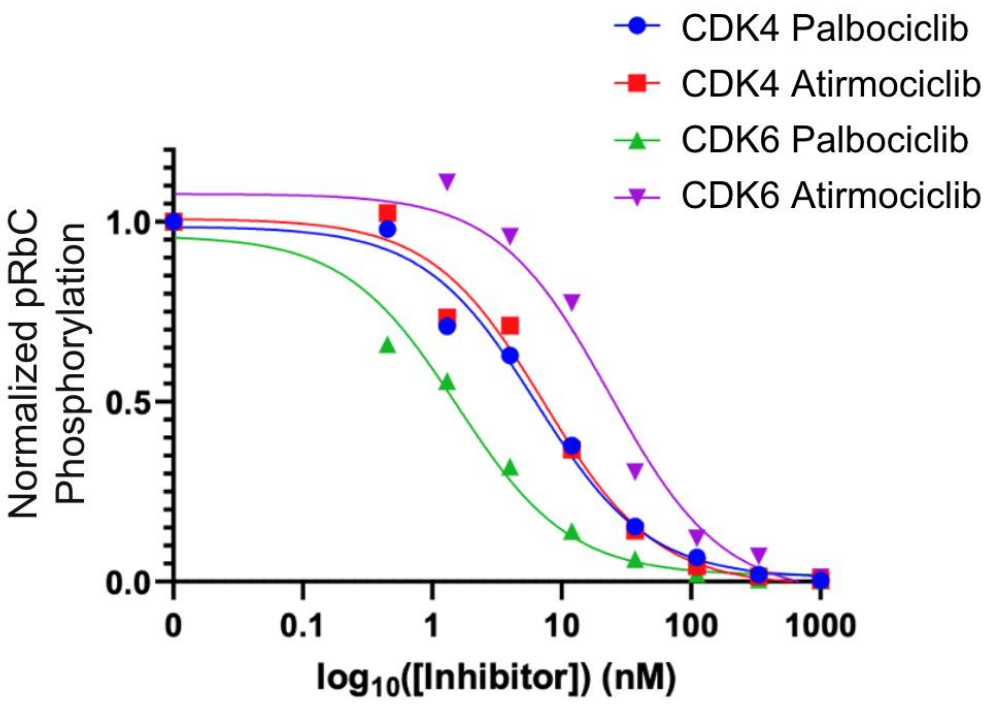


**Figure S11. Dose-response curves showing the effect of CDK4/6 inhibitors, palbociclib (PD 0332991) and atirmociclib (PF-07220060), on the phosphorylation of the retinoblastoma protein (pRbC) in CDK4 and CDK6 complexes.** The x-axis is the concentration of the inhibitors on a logarithmic scale, and the y-axis shows normalized pRb phosphorylation levels. Each curve represents a different condition: CDK4 with palbociclib (blue circles), CDK4 with atirmociclib (red squares), CDK6 with palbociclib (green triangles), and CDK6 with atirmociclib (purple inverted triangles). The data indicate that palbociclib is more selective for CDK6 over CDK4. In contrast, atirmociclib is more selective for CDK4 over CDK6.

**Table S1. Summary of the simulations of CDK4 and CDK6 complexes. The mutations of CDKs are shown in Table S2.**

| System | Label | Source PDB | Components | αC | A-loop | DFG | Simulation time (μs) | Number of replicas |
|---|---|---|---|---|---|---|---|---|
| Cyclin-D1/CDK4 (pT172) | $CDK4^{WT}$ | 7SJ3, 2W9Z | Cyclin-D1, CDK4 (pT172), ATP, $Mg^{2+}$ | in | extended | in | 2 | 3 |
| Cyclin-D1/CDK6 (pT177) | $CDK6^{WT}$ | 1XO2, 2W9Z | Cyclin-D1, CDK6 (pT177), ATP, $Mg^{2+}$ | in | extended | in | 2 | 3 |
| Cyclin-D1/$CDK6^{\Delta Cter}$ (pT177) | $CDK6^{\Delta Cter}$ | 1XO2, 2W9Z | Cyclin-D1, CDK6 (pT177), ATP, $Mg^{2+}$ | in | extended | in | 2 | 3 |
| Cyclin-D1/$CDK4^{\beta3-\alpha C(CDK6)}$ (pT172) | $CDK4^{\beta3-\alpha C(CDK6)}$ | 7SJ3, 2W9Z | Cyclin-D1, $CDK4^{\beta3-\alpha C(CDK6)}$ (pT172), ATP, $Mg^{2+}$ | in | extended | in | 2 | 3 |
| Cyclin-D1/$CDK6^{\beta3-\alpha C(CDK4)}$ (pT177) | $CDK6^{\beta3-\alpha C(CDK4)}$ | 1XO2, 2W9Z | Cyclin-D1, $CDK6^{\beta3-\alpha C(CDK4)}$ (pT177), ATP, $Mg^{2+}$ | in | extended | in | 2 | 3 |
| Cyclin-D1/$CDK4^{F93G}$ (pT172) | $CDK4^{F93G}$ | 7SJ3, 2W9Z | Cyclin-D1, $CDK4^{F93G}$ (pT172), ATP, $Mg^{2+}$ | in | extended | in | 2 | 3 |
| Cyclin-D1/$CDK6^{F98G}$ (pT177) | $CDK6^{F98G}$ | 1XO2, 2W9Z | Cyclin-D1, $CDK6^{F98G}$ (pT177), ATP, $Mg^{2+}$ | in | extended | in | 2 | 3 |

**Table S2. CDK4 and CDK6 and mutant sequences.** Altered sequences are underlined; delete sequence is denoted as red dash.

| Name | Sequence | Ending residue ID |
|---|---|---|
| **$CDK4^{WT}$** | -------MAT SRYEPVAEIG VGAYGTVYKA RDPH-SGHFV ALKSVRVPNG GGGGGGLPIS | 52 |
| **$CDK6^{WT}$** | MEKDGLCRAD QQYECVAEIG EGAYGKVFKA RDLKNGGRFV ALKRVRVQTG ---EEGMPLS | 57 |
| **$CDK6^{\beta3-\alpha C(CDK4)}$** | MEKDGLCRAD QQYECVAEIG EGAYGKVFKA RDLKNGGRFV ALKRVRVPNG GGGGGGMPLS | 60 |
| **$CDK4^{\beta3-\alpha C(CDK6)}$** | -------MAT SRYEPVAEIG VGAYGTVYKA RDPH-SGHFV ALKSVRVQTG ---EEGLPIS | 57 |
| **$CDK6^{\Delta Cter}$** | SALSHPYFQD LERCKE---------- | 308 |

## References


1. Letunic, I. and P. Bork, *Interactive Tree of Life (iTOL) v6: recent updates to the phylogenetic tree display and annotation tool.* Nucleic Acids Res, 2024. **52**(W1): p. W78-W82.